Simulation Models for Programmable Metallization Cells

by

David Ryan Oleksy

A Thesis Presented in Partial Fulfillment
of the Requirements for the Degree
Master of Science

Approved November 2013 by the
Graduate Supervisory Committee:

Hugh Barnaby, Chair
Michael Kozicki
Arthur Edwards

ARIZONA STATE UNIVERSITY

December 2013

ABSTRACT

Advances in software and applications continue to demand advances in memory. The ideal memory would be non-volatile and have maximal capacity, speed, retention time, endurance, and radiation hardness while also having minimal physical size, energy usage, and cost. The programmable metallization cell (PMC) is an emerging memory technology that is likely to surpass flash memory in all the listed ideal memory characteristics. A comprehensive physics-based model is needed to fully understand PMC operation and aid in design optimization.

With the intent of advancing the PMC modeling effort, this thesis presents two simulation models for the PMC. The first model is a finite element model based on Silvaco Atlas finite element analysis software. Limitations of the software are identified that make this model inconsistent with the operating mechanism of the PMC.

The second model is a physics-based numerical model developed for the PMC. This model is successful in matching data measured from a chalcogenide glass PMC designed and manufactured at ASU. Matched operating characteristics observable in the current and resistance vs. voltage data include the OFF/ON resistances and write/erase and electrodeposition voltage thresholds. Multilevel programming is also explained and demonstrated with the numerical model. The numerical model has already proven useful by revealing some information presented about the operation and characteristics of the PMC.

*Dedicated to my parents*

*Mr. Daniel Oleksy and Mrs. Linda Oleksy*

ACKNOWLEDGEMENTS

TABLE OF CONTENTS

LIST OF TABLES

## LIST OF FIGURES

NOMENCLATURE

CBRAM              conductive-bridging random-access memory

ChG                chalcogenide glass

DFT                density function theory

DRAM               dynamic random-access memory

ECM                electrochemical metallization

FEA                finite element analysis

FEM                finite element method

MOS                metal-oxide-semiconductor

NVM                non-volatile memory

PMC                programmable metallization cell

Redox              reduction-oxidation (chemical reactions)

ReRAM /RRAM        resistive random-access memory

TCAD               technology computer aided design

# 1. INTRODUCTION

## 1.1. Motivation for New Memory Technology

Today, the most popular type of non-volatile memory (NVM) is flash memory. For example, NAND-flash is commonly used in memory cards, USB flash drives, and solid-state drives. Advances in software and applications continue to demand advances in memory. The ideal memory would be non-volatile and have maximal capacity, speed, retention time, endurance, and radiation hardness while also having minimal physical size, energy usage, and cost. Most computers still use volatile main memory such as dynamic random-access memory (DRAM), because it operates at a much higher speed [1]. One of the primary drawbacks of DRAM is that it must be refreshed constantly, taking significant power, or the system state is lost. Computers and their sub-systems should be turned off to save energy when not in use; however, people tend to leave them on to avoid long booting times in which the operating system is loaded from slower NVM into the faster DRAM. NVM of comparable speed and endurance could supplement or eliminate DRAM and have the benefits of instant-on/off systems capability and greatly reduced energy usage. Each NVM cell could remain off while not being written or read whether the rest of the system is off or on. In an effort to shrink the gap between slow storage and fast RAM, flash memory technology has been greatly improved since its debut in 1984 as summarized in Table I with data from [2-4]. Nonetheless, it has not caught up to the speed or endurance of DRAM and maintaining endurance and reliability is an ever increasing challenge with technology scaling [5]. Furthermore, it is expected that down-scaling of metal-oxide-semiconductor (MOS) transistor-based memory, including DRAM and flash, will halt at a feature size of about

1

5-7 nm by year 2020-2025 due to a breakdown of the MOS operating physics [5]. There i

a growing interest in alternative memory technologies with the goal to surpass the

limitations of transistor memory [6-8] and offer other application opportunies such as

stochastic neuromorphic auditory and visual cognitive processing applications [9].

Table I:  Flash memory of 1984 versus 2013

| Year | Capacity (bits) | Density (bits/mm$^2$) | Write Speed (bits/s) |
|------|-----------------|------------------------|----------------------|
| 1984 | $2.56 \times 10^3$ | $7.74 \times 10^3$ | $1.00 \times 10^2$ |
| 2013 | $9.01 \times 10^{13}$ | $9.41 \times 10^8$ | $3.35 \times 10^{10}$ |

1.2.    Meet the PMC

One emerging research platform technology is the programmable metallization

cell (PMC), which is useful for applications in memory and beyond, such as self-healing

interconnects for flexible electronics [10], programmable threshold logic [11],

neuromorphic computing [9], micro-electromechanical systems [12], microfluidics [13]

and optics [14]. The PMC has been called many names based on its application including

conductive-bridging (CB) cell, conductive-bridging random-access memory (CBRAM),

resistive random-access memory (RRAM/ReRAM), memristor, electrochemical

metallization (ECM) cell (EMC), redox memory, solid-electrolyte memory, nano-ionic

memory, and Nanobridge. As the names suggest, the cell changes its resistance by

constructing and destructing a conducting bridge between two electrodes via

electrochemical reduction-oxidation (redox) reactions and ionic transport. The PMC is a

two-terminal switch with a high-resistance in the non-bridge off-state (OFF) and low-

resistance in the bridged on-state (ON). The bridge can be repeatedly constructed and destructed and is adequately stable in both states without static power dissipation, as with most NVM technologies. CBRAM is a commercially available PMC-based NVM that combines key features of flash and DRAM including small size (< 20 nm, Fig. 1), non-volatility (10 years at 70°C, Fig. 2), high endurance (> $10^6$ cycles, Fig. 3), multilevel programmability (Fig. 4) [15], fast random access speed (< 50 ns) [16], and very low energy usage as compared to Flash in Table II [17].
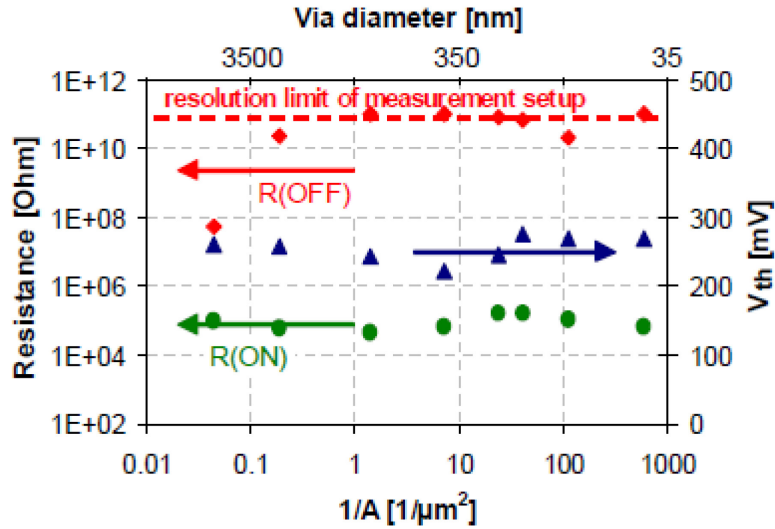


Fig. 1: Maintained switching ratio vs. cathode size demonstrates good PMC scalability
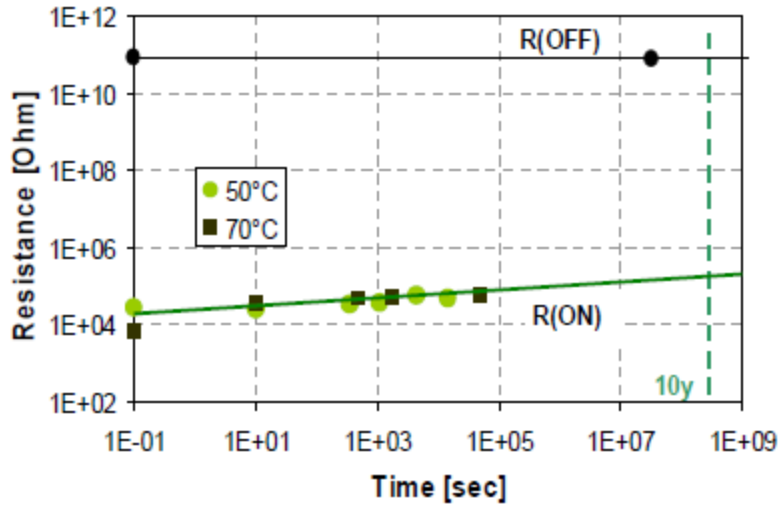
Fig. 2: Persistent on-state resistance at elevated temperatures demonstrates good PMC state retnetion time
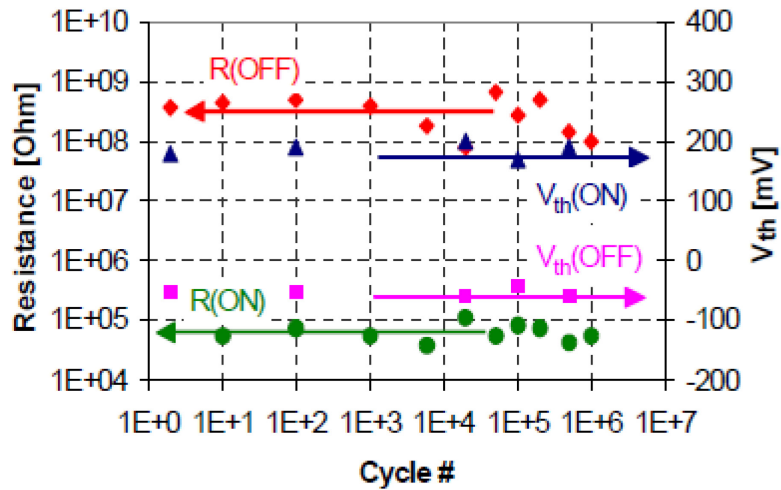


Fig. 3: Maintained switching ratio vs. cycle demonstrates good PMC endurance

4
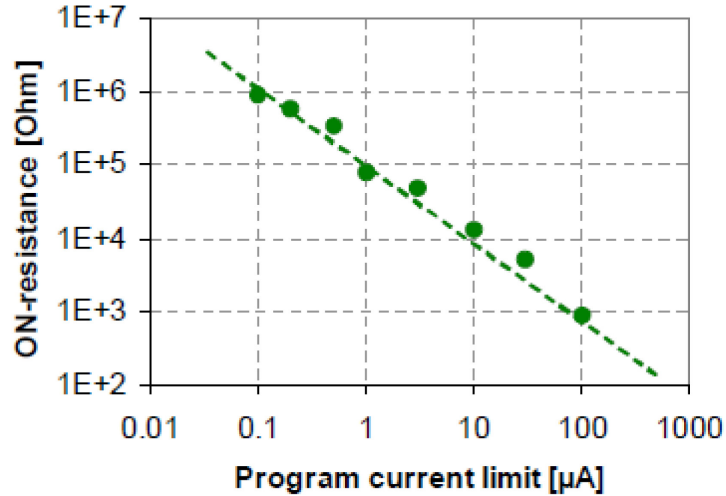
Fig. 4: On-state resistance vs. programming current demonstrates PMC multilevel programmability

Table II: Flash versus PMC energy usage

| Technology | Program Energy (J) | Erase Energy (J) |
|---|---|---|
| Flash cell | 5E-09 | 1.0E-08 |
| PMC | 3.4E-12 | 2.40E-13 |

While various PMC designs demonstrate favorable performance trends that suggest greater potential for widespread adoption, a comprehensive physics-based model has yet to be developed as noted in the latest International Technology Roadmap for Semiconductors report [5]. Such a model is needed to better understand PMC operation and aid in design optimization for better performance. The insight provided by that model would also allow the development of an accurate compact model for circuit simulation, which is necessary for efficient large scale circuit design with PMC devices. This thesis presents two simulation models for the PMC to advance the modeling effort. Chapter 2 provides material and device theory applicable to the PMC as well as some electrical data

5

and imagery of various filament types. Chapter 3 presents a novel approach to simulating the PMC in commercial finite element device simulation software. Chapter 4 presents a physics-based numerical model developed for the PMC with great success.

## 2. PMC THEORY

### 2.1. Structure and Materials of the PMC

The PMC typically has a three-layer structure of metal-insulator/electrolyte-metal (MIM/MEM), though designs with more layers do exist [8, 18]. An electrochemically active metal (e.g., Ag or Cu) is used for the anode while the cathode is relatively inert (e.g., Pt or W). Note that W forms compounds with Se, which is used in some electrolytes. The solid-electrolyte is an ion conductor and sometimes an electron insulator [19]. Many chemical compounds have been used as the solid-electrolyte, although they are mostly oxides or chalcogenides. A non-exhaustive summary of reported combinations of electrode and insulator/electrolyte materials is given in Table III [8]. Some materials used, such as $Ge_xS_y$ and $Ge_xSe_y$, start as insulators without mobile ions and become ionic or mixed (ionic and electronic) conductors containing mobile ions by a thermal, chemical, or photochemical doping process during fabrication or by an electrical forming process after fabrication [19]. Density functional calculations of Ag in $Ge_2Se_3$ have shown that isolated, interstitial Ag will auto-ionize by donating an electron to the conduction band, which enables the ionized Ag atom to transport in the presence of an electric field. This behavior is likely common in narrow-gap materials and insulators with large numbers of acceptor defect states in the gap [20].

Table III: Reported PMC material combinations

| Anode metal | Ag | Cu |
|---|---|---|
| Electrolyte | Cathode metal | |
| $Ge_xS_y$ | W | W |
| $Ge_xSe_y$ | W, Pt, Ni | W |
| Ge-Te | TiW | TaN |
| GST | Mo | |
| As–S | Au | |
| $Zn_xCd_{1-x}S$ | Pt | |
| $Cu_2S$ | | Pt, Ti |
| $Ta_2O_5$ | | Pt, Ru |
| $SiO_2$ | Co | W, Pt, Ir |
| $WO_3$ | W | W |
| $TiO_2$ | Pt | |
| $ZrO_2$ | Au | |
| GdOx | | W |

## 2.2.    Basic Operation of the PMC

The PMC exhibits bipolar operation meaning that it is switched ON (i.e., "set" or "programmed") and OFF (i.e., "reset" or "erased") with opposite polarities. The cell is programmed by applying sufficient positive voltage on the anode, which creates an electric field across the cell and causes the anode to oxidize at its interface with the middle, ion conducting layer. The cations are driven through the solid-electrolyte by drift and diffusion to the cathode where they meet an electron and reduce. The electrodeposition builds a dendritic structure that serves as a conductive filament between the cathode and anode, i.e., metallizing the cell. The filament can be broken with application of sufficient negative voltage on the anode and this cycle is repeatable.

8

The on-state resistance can vary by orders of magnitude depending on the robustness of the bridge, which depends on the programming compliance current limit [21]. A higher programming current creates a more robust bridge, which makes the resistance smaller. The PMC is typically tested by setting a current limit and sweeping the voltage to a value greater than the OFF/ON switching threshold voltage for the particular PMC. The bridge will form at this threshold voltage and continue to increase its girth which decreases the resistance until the voltage falls below the threshold for electrodeposition ($V_{fwd}$). Because the compliance current limit, $I_{comp}$, and $V_{fwd}$, are fixed, the set resistance will be

$$R_{set} = V_{fwd}/I_{comp} \qquad (1)$$

according to Ohm's law. There may be some slight variance in $V_{fwd}$ due to random variations in fabrication. The resistance can be measured without switching its state by applying a small positive voltage on the anode and measuring the current.

The electrical input for a standard test of a real PMC is a double DC voltage sweep from -1V to 1V and back to -1V using a semiconductor parameter analyzer. The DC sweep is actually a specified amount of time spent at discrete voltage steps such as 1 ms at 1 mV increments from 0 to 1V. This measurement is actually quasi-DC or transient. The frequency of a DC signal is 0 Hz, which means that it never changes. In the provided example, the voltage is changing every millisecond. The voltage sweep rate, and even DC, can affect the behavior of the PMC, because it depends on the history of charge flow. In simulation, DC sweeps are truly DC since it is just a calculation.

Consequently, PMCs should not typically be simulated with DC sweeps. Rather, a transient voltage ramp simulating a real quasi-DC sweep is more appropriate.


2.3.    Electrical Data

Current versus voltage (I-V) and resistance versus voltage (R-V) data recorded from an Arizona State University (ASU) ChG PMC is plotted in Figs. 10-12. The data come from two successive measurements of a single device recorded by an Agilent 4156C Precision Semiconductor Parameter Analyzer. The test performed is a double DC voltage sweep from -0.5V to 0.5V and back to -0.5V with 5 mV steps at a rate of 1 V/s and a compliance current limit of 50 µA. The PMC is initially OFF, switched to ON and then returned to OFF. The write and erase threshold voltages for this device are approximately 150 mV and -60 mV, respectively. The OFF resistances are 59.5 MΩ and 36.6 MΩ at 10 mV for the first and second tests, respectively. The ON resistances are 37.3 kΩ and 26.2 kΩ at 10 mV for the first and second tests, respectively. The first and second OFF/ON resistance ratios are 1.60E3 and 1.40E3, respectively. Note that when the current is at the 50 µA limit the displayed voltage continues along the set DC sweep, but the actual voltage is reduced. The R-V data in Fig. 7 is calculated with the displayed voltage and is therefore erroneous where the current is limited.
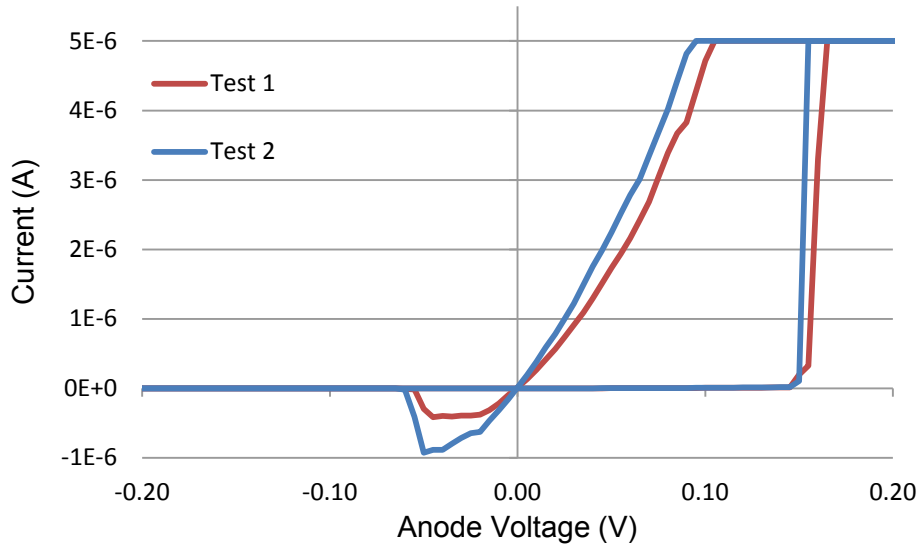
Fig. 5: ASU PMC I-V characteristic on a linear y-scale
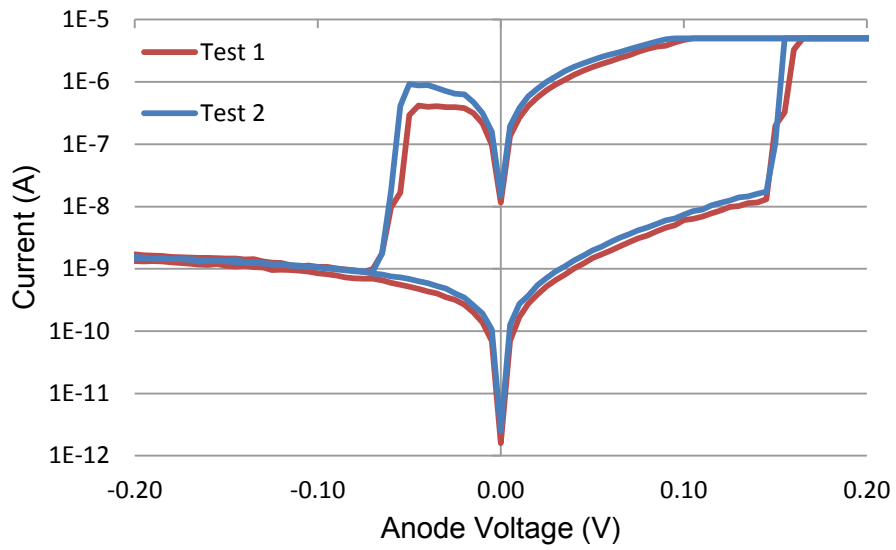


Fig. 6: ASU PMC I-V characteristic on a logarithmic y-scale
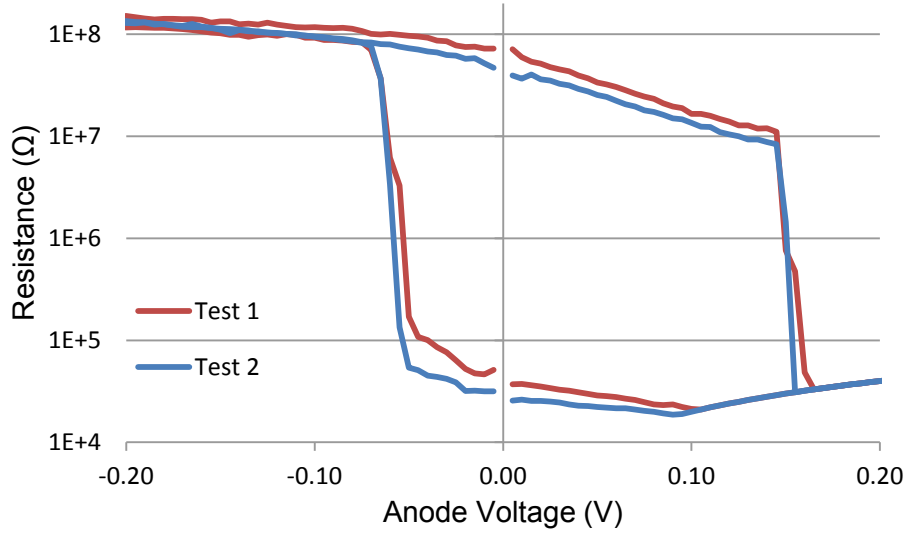
Fig. 7: ASU PMC R-V characteristic on a logarithmic y-scale

2.4.    Electrode Current

In the on-state, current is primarily due to electron flux through the metallic filament. Current in the off-state is mostly charge transfer caused by oxidation and reduction of the active metal at the electrodes.  Charge transfer refers to the active metal ions transferring from the electrodes into the electrolyte or vice versa. For example, an Ag atom on an electrode can become a cation by oxidation and then transfer into the electrolyte over an energy barrier. The current density of the charge transfer can be described by the Butler-Volmer equation [22, 23]:

$$j_{BV} = j_0 \left[ exp\left( \frac{\alpha z e \eta}{kT} \right) - exp\left( -\frac{(1-\alpha)z e \eta}{kT} \right) \right] \tag{2}$$

where $j_0$ is the exchange current density, $\alpha$ is the transfer coefficient, $ze$ is the ion charge, $\eta$ is the electrochemical overpotential, and $kT$ is the thermal energy. Equation (2) applies at each electrode with two components; i.e., the anodic and cathodic components. The

12

first and second terms of (2) are the anodic and cathodic currents, respectively. Anodic

partial current is the flow of positive charge into the electrolyte from the electrode

whereas cathodic current flows in the opposite direction. In equilibrium, the anodic and

cathodic currents cancel, and the magnitude of each is the exchange current.
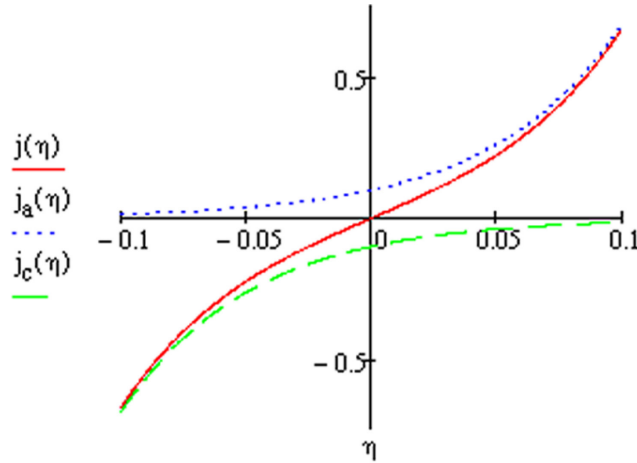


Fig. 8: Butler-Volmer electrode current versus overpotential. The anodic and cathodic components are shown as $j_a(\eta)$ and $j_c(\eta)$, respectively. The total electrode current is symmetric because the transfer coefficient α was set to 0.5 for demonstration.

2.5.    Ion Transport

Ions in the electrolyte need to transport and reduce at the cathode in order to build

the conductive filament. Transport of the ions is driven by electric field and thermally

activated ion hopping between adjacent sites which is described by the model of Mott and

Gurney [24, 25]. The ionic hoping current density as a function of electric field in the

case of a symmetric energy barrier $W_a$ is given by [22, 25, 26]:

$$j_{hop} = 2zecaf\left(-\frac{W_a}{kT}\right)\sinh\left(\frac{E \cdot ze \cdot a}{2kT}\right) \tag{3}$$

where $c$ is the concentration of mobile ions with charge $ze$, $a$ is the hoping distance, $f$ is the attempt-to-escape frequency, $W_a$ is the activation energy, $E$ is the electric field, and $kT$ is the thermal energy.

2.6.    Filament Structure

The first known report of a PMC was published in 1976 with the title "Polarity-dependent memory switching and behavior of Ag dendrite in Ag-photodoped amorphous $As_2S_3$ films" [27]. In addition to characterizing a vertical three-layer PMC, they also fabricate and test a coplanar PMC for the purpose of visually observing the switching phenomena. They observed the forming of the Ag filament through a microscope. A photomicrograph just after the filament bridged the electrodes and the device abruptly switched to low-resistance is shown in Fig. 9 from [27].  It clearly shows that the filament is dendritic; that is, the filament branches like a tree, especially at the top (Ag side) where the electrolyte was partially photodoped. The photodoped region contains a high concentration of Ag unlike the non-photodoped region. The non-photodoped region yields a sampling dendrite; i.e., a medium amount of branching, or sampling of the surroundings, as dominant growth continues in a single selective direction. The photodoped region yields more of a space-filling dendrite; i.e., a high amount of branching that fills the space. The distance between the electrodes is not mentioned, but it is likely on the order of micrometers or larger, which is much larger than the common nanometer range thickness of PMCs today. The PMC was then switched OFF with a reverse bias, but no change in the filament was observable by visual inspection.

14
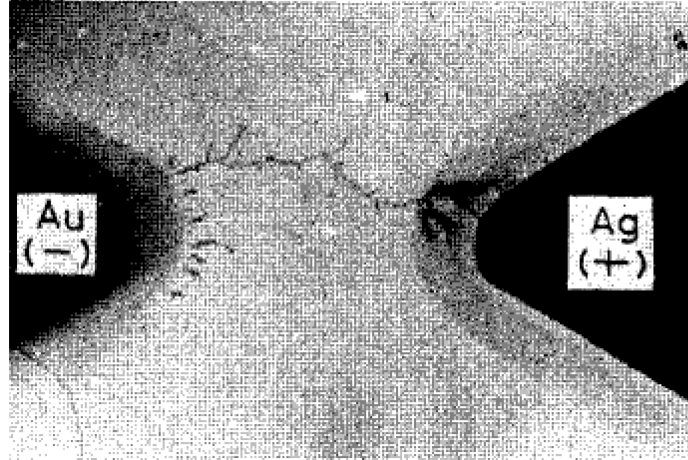
Fig. 9: Micrograph of Ag dendrite in coplanar Ag/As$_2$S$_3$/Au PMC

A study published in 2007 provides scanning electron microscope (SEM) images of a coplanar Ag/H$_2$O/Au PMC [28]. The gap between the electrodes is 3 μm, and a drop of deionized water fills the gap to serve as the ionic transport medium. This structure yields greater space-filling dendrites as shown in Fig. 10 from [28]. The image resolution was not high enough to resolve the fine structure at the point of contact with the anode, but the authors believe that only one "nano-twig" at the top of the dendrite connects to the Ag electrode. An electrostatic potential simulation of the "nano-twig" reveals that the potential-drop and field is greatest at the narrowest part of the filament as shown in Fig. 11 from [28]; thus, this is the point of dissolution when the PMC is switched OFF. No images are provided after switching OFF, and thus it may be safe to assume that the remaining vast majority of the dendrite did not dissolve.

15
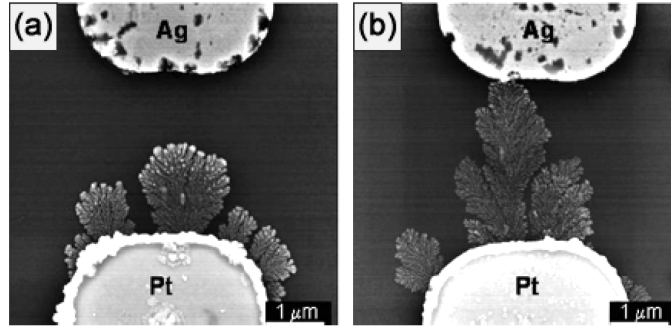
Fig. 10: SEM images of space-filling dendrite in coplanar Ag/H$_2$O/Pt PMCs after applying one volt to the Ag electrode for (a) two seconds and (b) four seconds
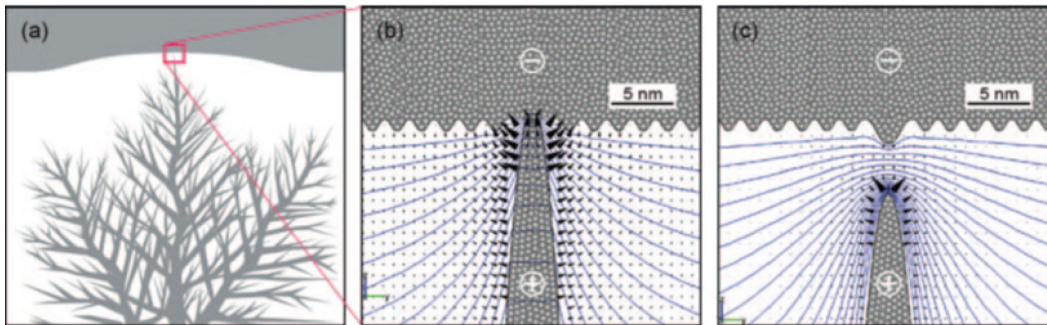


Fig. 11: Electrostatic potential simulation of dendrite tip while switching OFF: (a) Sketch of dendrite and anode. (b) Tip of dendrite in higher magnification, representing the situation just before dissolution. After applying -200 mV on the anode, the blue equipotential lines are 10 mV from each other. The black cones represent the electrical field and direction of Ag$^+$ ion drift. (c) The dendrite retreats due its dissolution. As soon as the electrical contact is severed, the field distribution changes and accelerates dissolution of the dendrite tip.

A study published in 2010 provides SEM images of a coplanar Ag/TiO$_2$/Pt PMC shown here in Fig. 12 [29]. The gap between the electrodes is less than 700 nm. Although the electrode gap is much smaller than the previous examples, the threshold voltage for switching on is much larger; presumably, this is due to the different insulator/electrolyte material properties. The forming switch is established when the filament is created for the first time. The SEM image provided in Fig. 12(a) was taken after the forming switch. This image and additional transmission electron microscopy (TEM) images show that

16

filament had broken up into non-connecting Ag spheres with an average diameter of about 8 nm. It is deduced that the filament was continuous upon bridging and then separated into spheres based on the I-V measurements provided in Fig. 12(b) in which the second voltage sweep begins within one second after the forming switch. If the filament had remained as it was upon forming, then the PMC would be ON from the beginning of the second sweep. Instead, the PMC switched OFF on its own and then switched ON again at a lower voltage during the second sweep. Rayleigh instability is the given reason why the nano-filament separated into spheres. Although an image of the filament in the supposed continuous state is not provided, it would seem that no significant branching occurred. This type of filament is a selective dendrite.
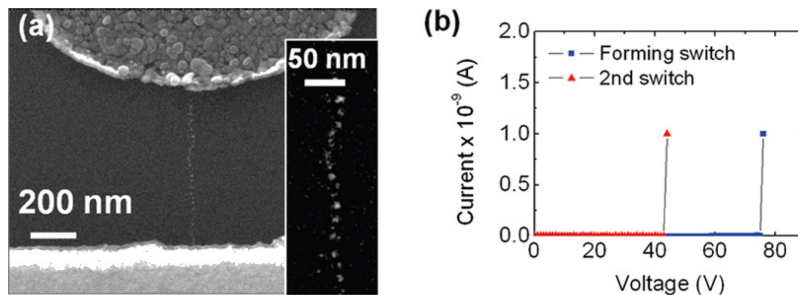


Fig. 12: SEM image of coplanar Ag/TiO$_2$/Pt PMC after first on-switch, and corresponding current-voltage measurement of the first and second on-switch

The preceding three examples of PMC Ag filaments show that not all filaments are created equal. The first PMC (Fig. 9) has a sampling dendrite in the non-photodoped (insulator) region and more of a space-filling dendrite in the photodoped (electrolyte) region. This dendrite is largest at the anode. The second PMC (Fig. 10) has space-filling dendrites in a liquid insulator (H$_2$O) that are smallest at the anode. The third PMC (Fig.

17

12) has a selective dendrite in a solid insulator (TiO$_2$). The different dimensions and materials between the three coplanar PMCs must cause different filament forming kinetics. This presents a challenge in making a comprehensive PMC simulator that can emulate an assortment of materials over a wide range of dimensions. At this point, it may be helpful to selectively reduce the PMC design and study space to a narrower range of materials and size. For example, thinner electrolytes might produce dendrites that are more selective, which could simplify the modeling.

# 3. FINITE ELEMENT MODEL

## 3.1. Finite Element Method

Simulating semiconductor devices based on fundamental physics involves solving charge carrier statistics and carrier transport differential equations including the continuity, drift-diffusion, and Poisson equations. A device is represented by a boundary value problem in which the behavior of charge carriers in the domain are governed by the aforementioned differential equations with additional restraints called boundary conditions around each of the material's boundaries. Electrical inputs, such as voltage and current, comprise some of the boundary conditions. A simulation of the device is a solution to the coupled differential equations that also satisfies the boundary conditions. The finite element method (FEM) is a numerical technique in mathematics for solving boundary value problems which divides the domain into many smaller domains called finite elements. Using many simple element equations for the finite elements allows for approximation of the more complex equation over the whole domain.

Atlas is a commercial semiconductor device simulation framework from Silvaco that utilizes FEM. This finite element analysis (FEA) software provides Device Technology CAD (Device TCAD), which enables device technology engineers to simulate the electrical, thermal, and optical behavior of semiconductor devices. The process of simulating a semiconductor device in Atlas basically consists of defining the structure, finite element mesh, materials and properties, behavior models, electrical inputs, and then the simulation runs while the materials and mesh remain fixed in position.

3.2.     Finite Element Model Implementation

Finite element simulations are performed with Silvaco Atlas on a two-dimensional structure representative of a three layer PMC. Fig. 13 shows the structure with the anode, electrolyte and cathode layers from top to bottom. The ChG film electrolyte is modeled as a wide bandgap semiconductor. Table IV reports the material constants used for the electrolyte and electrodes, which were extracted from data reported in [30] and obtained from density functional theory (DFT) calculations [31].
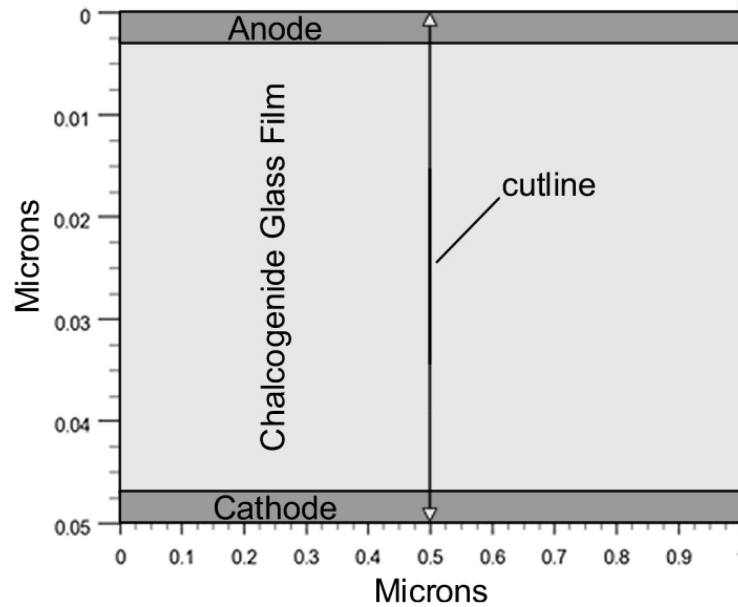


Fig. 13:  Two dimensional FE simulation structure

Table IV: Material constants used in Atlas simulation

| ChG bandgap | 2.5 eV |
|---|---|
| ChG relative permittivity | 5.0 |
| ChG affinity | 3.45 eV |
| Anode work function | 4.6 eV |
| Cathode work function | 4.2 eV |

Atlas solves standard carrier statistics and transport equations for semiconductors. Additional models are utilized to simultaneously perform ion transport and reaction calculations on the structure. Continuity equations for the model are expressed analytically as

$$\frac{dN_{Ag^+}}{dt} = -\left(\nabla F_{Ag^+}\right) - \left(R_{Ag^+}\right) + \left(G_{Ag^+}\right) \tag{4}$$

$$\frac{dN_{Ag}}{dt} = -\nabla F_{Ag} - R_{Ag} + G_{Ag} \tag{5}$$

$$\frac{dn}{dt} = -\nabla F_n - R_n - G_n \tag{6}$$

where $N_{Ag}{}^+$, $N_{Ag}$, and $n$ are the concentrations of $Ag^+$, neutralized Ag, and electrons, respectively. The flux for each charged species, i.e., parameter $F_X$ in equations (4-6), are obtained from the drift-diffusion equations

$$F_{Ag^+} = -\left(D_{Ag^+}\right)\left(\frac{q\nabla\Psi}{kT} + \nabla N_{Ag^+}\right) \tag{7}$$

$$F_{Ag} = -D_{Ag}\nabla N_{Ag} \tag{8}$$

$$F_n = -D_n\left(-\frac{q\nabla\Psi}{kT} + \nabla n\right) \tag{9}$$

where $D_{Ag^+}$, $D_{Ag}$, and $D_n$ are the diffusion constants for $Ag^+$, neutralized Ag, and electrons, respectively, and $\Psi$ is the potential within the simulated electrolyte. The $Ag^+$ diffusion constant is estimated from first principles calculations using the diffusivity approximation

$$D = a^2 f exp\left(\frac{-W_A}{kT}\right) \tag{10}$$

where $a$ is the average hopping distance of the particle, $f$ is the attempt to escape frequency, and $W_A$ is the activation energy for hopping. $E_A$ comes directly from atomistic calculations using the nudged elastic band method [32]. Preliminary investigations of interstitial $Ag^+$ in a crystalline model of $Ge_2Se_3$ indicates activation energies greater than 2.5 eV within the layer while transport along the layer surfaces has much lower activation energy of approximately 0.5 eV. The attempt-to-escape frequency is taken from vibrational calculations showing approximately $5x10^{-11}$ $s^{-1}$. The hopping distance is approximately 7 Å. Plugged into (10), these predict a diffusivity of about $1.0x10^{-11}$ $cm^2/s$ at room temperature. The recombination and generation terms in equations (4-6) capture the kinetics of the forward and reverse chemical reactions expressed as

$$Ag^+ + e^- \leftrightarrow Ag \tag{11}$$

The forward and reverse reactions are described by (12) and (13), respectively.

$$R_{Ag^+} = R_n = G_{Ag} = k_{Fwd} exp\left(\frac{-W_{AFwd}}{kT}\right)\left(N_{Ag^+}\right)(n) \tag{12}$$

$$G_{Ag^+} = G_n = R_{Ag} = k_{Rev} exp\left(\frac{-W_{ARev}}{kT}\right)\left(N_{Ag}\right) \tag{13}$$

The forward and reverse reaction rate coefficients, $k_{Fwd}$ and $k_{Rev}$, and forward and reverse activation energies, $W_{AFwd}$ and $W_{ARev}$, are also estimated using the first principles, DFT calculations.

### 3.3.    Generic Ion Model Explained

Atlas allows for doping profiles of species to be defined for the generic ion transport and reaction models where the species are neutral and charged particles that can react with each other and free carriers. For a PMC, a neutral species (sp0) could represent Ag, and a +1 charged species (sp1) could represent $Ag^+$. To serve as the source of $Ag^+$, the structure is initially doped with sp1. A built-in electric field due to the electrode work function difference forces sp1 toward the anode in equilibrium. Initial equilibrium yields a highly sloped sp1 doping profile within the electrolyte with greatest concentration next to the anode as shown in Fig. 14 [31].
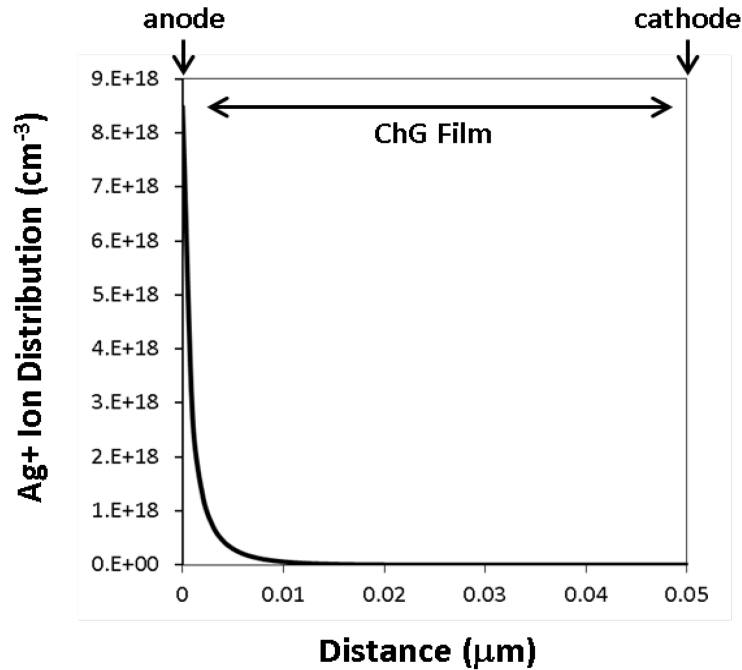
Fig. 14: Distribution of Ag$^+$ in equilibrium along vertical center cutline

Upon applying a voltage greater than the write threshold voltage to the anode, sp1 begins to transport toward the cathode. The required process from there is to have sp1 meet an electron at the cathode to recombine with and form sp0, representative of neutral Ag. Subsequent sp1 should then be able to recombine upon reaching the newly formed sp0. That process should repeat thereby forming a bridge of sp0 from the cathode back to the anode.

Unfortunately, the species cannot behave as required to simulate PMC operation. The species can only transport, react with other species and free carriers, and simply exist as arbitrary neutral or charged dimensionless particles. The species exist in concentration rather than as individual particles that fill discrete spaces and the species cannot react with the device materials. Therefore, the species are not capable of forming any type of phase, conductive or not, which is required for the filament.

24

There is another problem even if the species could form regions of greater conductance. The long-rage disorder in ChG solid-electrolyte provides fast transport channels for $Ag^+$ [22]. Those channels would determine the possible routes of $Ag^+$ and, consequently, possible shapes of the filaments. Atlas cannot simulate those channels for the species to navigate and fill. Unlike Ag in nano-voids, the species move unrestricted in location, and their concentration gradients are relatively gradual.

Atlas performs some computational physics that need to be applied to the PMC such as standard carrier statistics and carrier transport; however, its generic ion transport and reaction model currently has shortfalls making it incapable of simulating a PMC. Atlas is not made to simulate electrochemical devices, such as the PMC, in which metal is rearranged. No FEA software has been reportedly developed for a PMC as of yet.

3.4.    Generic Ion Model Workaround

A workaround was devised to address the non-conductance of sp0, which is the neutral species representing neutral Ag in the electrolyte. First, a bit more explanation of the simulation in Atlas is necessary. Atlas has a transient solution mode which is used to simulate the quasi-DC measurement as discussed in Chapter 2.2. Like the quasi-DC measurement, a transient simulation is a series of small voltage steps over time. The transient setup is defined by the initial and ending voltage, total ramp time, and a maximum time step between voltage steps. A solution is calculated at each voltage-time step. The voltage increment between solutions is not explicitly defined. The time step (and voltage step) may be dynamically reduced if the solution does not converge with the maximum step. If the generic ion model could produce a conductive filament, then

simulation of the PMC switching on would consist of a single voltage-time sweep. Because sp0 is not conductive, a workaround is necessary to add something conductive in place of sp0 as it occurs. The conductance of the filament is important even before the electrodes are bridged, because as the filament shrinks the distance between the electrodes the electric field increases even with a constant voltage applied. In turn, the growth rate and selectivity of the dendrite are expected to increase.

The idea of the workaround is to split the single transient simulation into many transient simulations. Then, n-type dopants (donors), serving as the conductive material, can be added to match the doping profile of sp0. The result is that a bridge of donors is grown across the electrolyte. While this is not equivalent to the precise nature of neutral Ag in the film, the conversion does effectively reduce the resistance across the film as sp0 grows with increasing anode voltage. Inserting metal instead of donors would seem like a better option, but that is not an option in Atlas. All metal is simulated as ideal metal, which means it has no resistance. While that could possibly work during vertical filament growth, the simulation would prematurely cease upon bridging. Only one electrode would exist at that time, and Atlas requires two or more electrodes. There are several pieces required for this multipart simulation including, an initial input deck, a running input deck, a Python script to generate doping profiles from the output structure files, an AWK script to update the running deck, and another Python script to bring these pieces together for an automated multipart simulation. Appendix A describes the multipart simulation in greater detail and provides the codes.

## 3.5.    Simulation Results

The finite element model multipart transient simulation is performed by increasing the voltage on the anode in 0.1V increments up to 0.9V while the cathode is fixed at 0V. The voltage ramps up in 1 $\mu$s and is held at each increment for 10 $\mu$s. The sp1 ($Ag^+$) concentration at voltages of 0V, 0.2V, 0.4V, 0.6V, and 0.8V along the vertical, center cutline are plotted in Fig. 15 [31]. The ions drift away from the anode with increasing voltage and begin to accumulate at the cathode interface between 0.2 and 0.4V. An additional simulation ramping down the voltage to 0V shows that the ions return to their equilibrium distribution within 100 $\mu$s. It should be noted that the transport times are highly dependent on the diffusion constants in equations (7–9). Refinements on the first principles calculations and parametric extraction from experimental data may lead to adjustments of the diffusivity values [31].
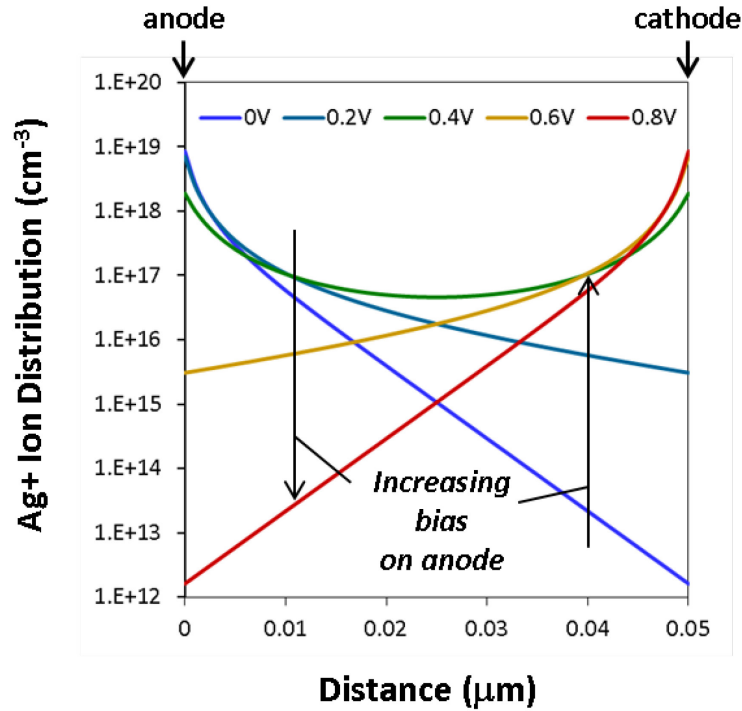
Fig. 15: Ag$^+$ distribution with increasing anode voltage and cathode fixed at 0V

The evolution of sp0 and donor (neutral Ag) concentration versus anode voltage is plotted in Fig. 16 [31]. The figure shows a significant rise in the concentration and evidence of species accumulation at the cathode interface for voltages above 0.4V. Note that the concentrations are uniform across the width of the structure instead of forming a thin dendrite. As explained in Chapter 3.3, the FEA software is not able to accurately model the dendritic bridging mechanism.
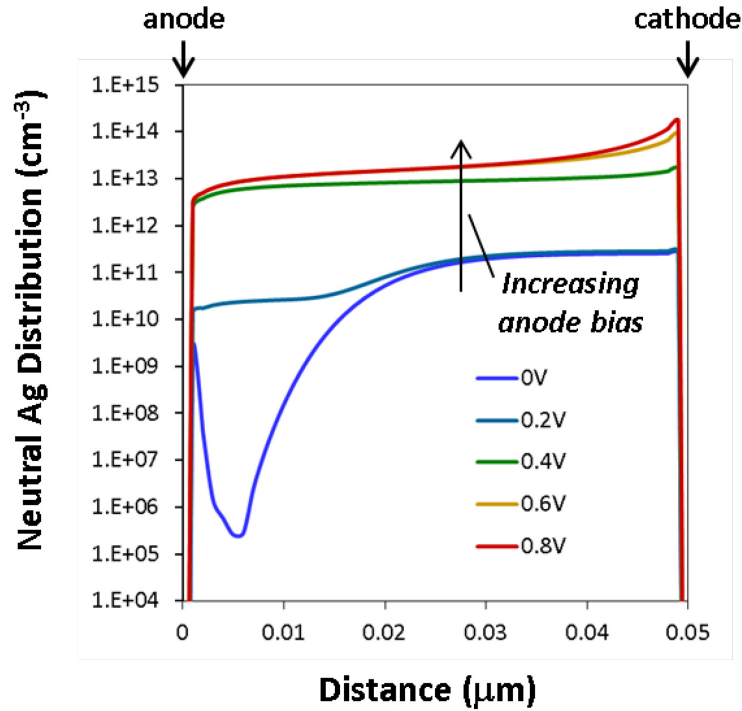
Fig. 16: Ag distribution with increasing anode voltage and cathode fixed at 0V

Fig. 17 plots the resistance versus anode voltage during the simulated voltage sweep [31]. The resistance before programming is greater than 1 GΩ. The resistance exhibits an exponential decrease during the voltage sweep up to 0.4V. Above 0.4V, the change in resistance becomes linear and reaches approximately 300 kΩ at 0.9V. Further simulation reveals that this low resistance level is maintained when the anode is returned to 0V. Although the resistance does decrease orders of magnitude, comparison with the measured R-V data in Fig. 7 reveals the difference in bridging kinetics. The ASU PMC has a discontinuous change in resistance while the finite element model has a continuous change in resistance. A discontinuous change in resistance indicates a low resistance filament forming through a high resistance film. The large, discontinuous step in resistance occurs when the filament connects or disconnects the anode and cathode. A

29

continuous change in resistance indicates that the film is changing from anode to cathode

all together; i.e. there is no filament growing from one electrode to the other.
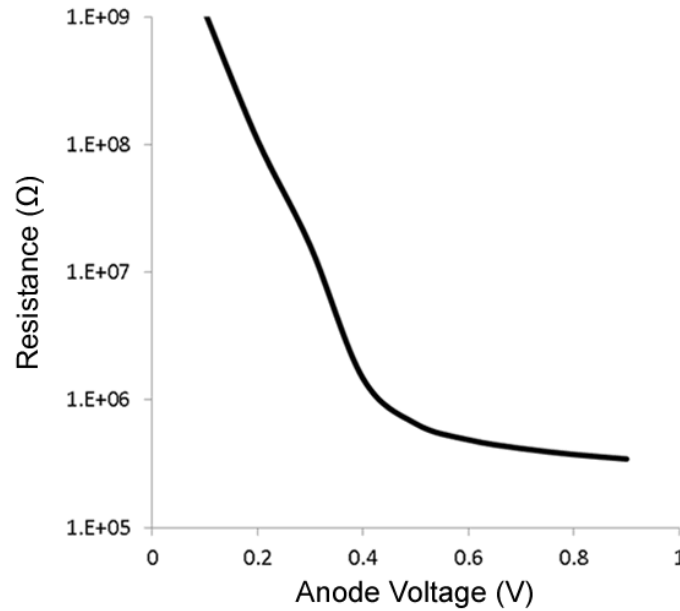


Fig. 17: R-V characteristic of finite element model

Fig. 18 plots the anode I-V as the anode voltage increases from 0V to 0.9V and

then returns to 0V [31]. The I-V response of the structure shows that the simulation

models the hysteresis characteristic of resistive NVM. These results show that during the

upward "write" sweep, the resistance changes from a high to low state (i.e., low to high

current), and when the anode is returned to 0V the low resistance state is saved. Unlike

the measured I-V data in Fig. 5, there is no current limit in the finite element model. Even

with limited current, the finite element model's I-V characteristic would remain

inconsistent with that of the ASU PMC due to the aforementioned difference in bridging

kinetics. The current would not discontinuously jump up to the current limit. The

30

resistance upon entering current limiting would remain approximately constant, and the current would come down from the limit at about the same point it entered.
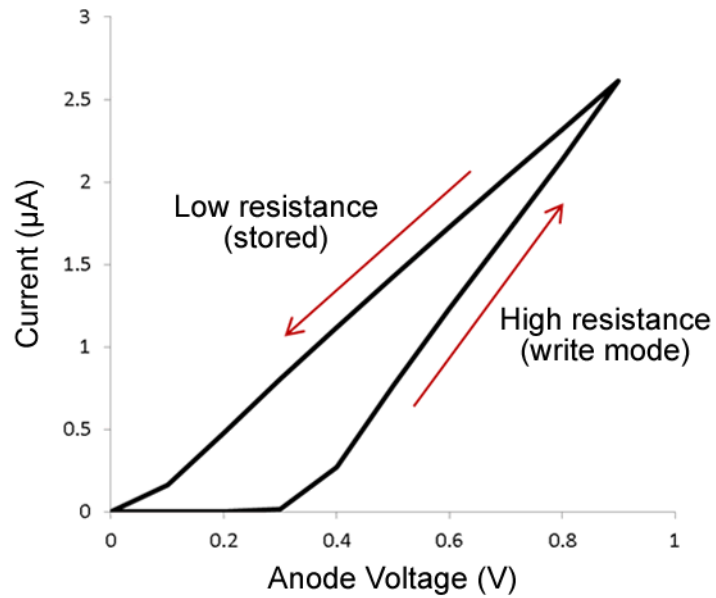


Fig. 18:  I-V characteristic of finite element model

The simulation results of the finite element model with generic ion transport and reactions in conjunction with the workaround and standard carrier statistics and transport equations are shown to effectively model some type of resistance change NVM, but the model is vastly inconsistent with the switching behavior of the ASU ChG PMC.

# 4. NUMERICAL MODEL

## 4.1. Numerical Method

A physics-based numerical model has been developed specifically for the PMC. A numerical model is required to simulate with arbitrary voltage inputs because the PMC has a complex hysteresis. Development of this model began as a reproduction of the model described in [26] and was then significantly improved upon. The model is written in m-code for Octave or MATLAB and uses a time-stepping procedure with analytical equations to obtain the model's behavior over time. The Mott and Gurney ionic hopping current (3) is assumed to be the rate limiting process in the PMC. Therefore, the Butler-Volmer charge transfer equation is not incorporated, but it could be if found necessary. All of the ionic flux is assumed to reduce on the filament, which is modeled as a cylinder with adjustable height and radius. The filament height is adjusted each time step in proportion to the ions accumulated during the step and the concentration of neutralized ions in the filament. The radius can change once the filament has connected the anode and cathode. The operating mechanism of the PMC model is visualized in Fig. 19. The filament height and radius along with material properties are used to calculate the non-ohmic resistance of the cell at each time step. A single equation is used to calculate the resistance independent of OFF/ON state. Current limiting is implemented in the model to simulate standard testing as with the Agilent 4156C. The numerical routine checks for errors within each time step, such as the current compliance or filament overgrowth, and dynamically adjusts the time step for precise and quick solutions.
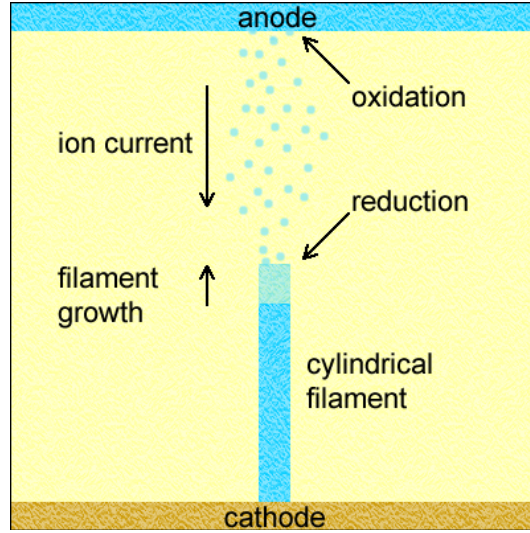
Fig. 19: Operating mechanism of PMC model

4.2.    Structure and Resistance Model

The resistance model calculates the total resistance of the PMC given the

dimensions and material properties of the cell and filament. The simulation structure is

modeled after an ASU PMC that is a cylindrical cell with a diameter of 5 μm and a ChG

electrolyte thickness of 60 nm. The height and radius of the filament are variables during

the simulation. As can be seen in the I-V data in Figs. 10–11, the PMC has a diode

characteristic in the OFF and ON states. The electrolyte and filament are modeled as

separate diodes in parallel. The resistances of the diodes are calculated using the

Shockley ideal diode equation with quality factor and added series resistance. The

electrolyte series resistance is given by

$$R_{se} = \rho_e \cdot L / (\pi \cdot (r_{cell}^2 - r^2)) \tag{14}$$

where $\rho_e$ is the resistivity of the electrolyte, $L$ is the electrolyte thickness, $r_{cell}$ is the radius

of the PMC, and $r$ is the radius of the filament. The series resistance of the filament (15)

is calculated as two resistors in series – the resistance of the neutralized ion portion of the filament and the resistance of the electrolyte in the cylindrical space remaining between the filament and the anode.

$$R_{sf} = (\rho_f \cdot h + \rho_e \cdot (L - h))/(\pi \cdot r^2) \tag{15}$$

where $\rho_f$ is the resistivity of the filament and $h$ is the height of the filament. The resistances of the electrolyte and filament diodes are given by (16) and (17), respectively, where $V$ is the applied anode voltage. An insignificant value, $10^{-16}$, is added to the diode current to avoid a division by zero error.

$$R_f = V \cdot \left[ I_{sf} \cdot \left( \exp\left(\frac{V}{n_f kT}\right) - 1 \right) + 10^{-16} \right]^{-1} + R_{sf} \tag{16}$$

$$R_e = V \cdot \left[ I_{se} \cdot \left( \exp\left(\frac{V}{n_e kT}\right) - 1 \right) + 10^{-16} \right]^{-1} + R_{se} \tag{17}$$

The total resistance of the PMC (18) is the parallel combination of (16) and (17).

$$R = \left( R_f^{-1} + R_e^{-1} \right)^{-1} \tag{18}$$

Table V summarizes the parameter values used in these equations. The filament material is assumed to be $Ag_2Se$ for which the resistivity was extracted from [33]. The other values besides the dimensions where chosen to approximately fit (18) with the data in Fig. 6.

Table V: Parameters for structure and resistance

| Parameter | Value | Unit | Description |
|---|---|---|---|
| $\rho_f$ | 7.0E-4 | $\Omega \cdot cm$ | Filament resistivity |
| $\rho_e$ | 8.0E4 | $\Omega \cdot cm$ | Electrolyte resistivity |
| $L$ | 6.0E-6 | cm | Electrolyte thickness |
| $r_{cell}$ | 2.5E-4 | cm | Cell radius |
| $I_{sf}$ | 1.8E-6 | A | Reverse saturation current |
| $I_{se}$ | 1.4E-9 | A | Reverse saturation current |
| $n_f$ | 1 | none | Diode quality factor |
| $n_e$ | 2 | none | Diode quality factor |

## 4.3. Filament Growth

The filament grows and dissolves according to the flux of $Ag^+$ ($j_{hop}$) given by (3) and the concentration of Ag in the filament. However, polarity dependent activation energy is used in (3) to account for the asymmetric OFF/ON switching voltages seen in Chapter 2.3. An asymmetric energy barrier is suggested in [34] as a possible cause for this behavior. The electric field used in (3) is given by (19).

$$E = V/(L + h \cdot (\rho_f/\rho_e - 1)) \tag{19}$$

The temperature of the cell, used in (3), (16) and (17), is given by [35] as

$$T = T_0 + V^2 R_{th}/R \tag{20}$$

where $T_0$ is the equilibrium temperature, $V$ is the applied anode voltage, $R_{th}$ is the equivalent thermal resistance and $R$ is the total cell resistance. The concentration of Ag in the $Ag_2Se$ filament is given by

$$N_{Ag} = 2N_A \cdot \rho_{Ag_2Se}/m_{Ag_2Se} \tag{21}$$

where $N_A$ is the Avogadro constant, and $\rho_{Ag_2Se}$ and $m_{Ag_2Se}$ are the density and molar

mass of Ag$_2$Se, respectively. When the PMC is non-bridged, the growth velocity of the

cylindrical filament height is given by

$$v_h = j_{hop}/(zqN_{Ag}) \tag{22}$$

When the PMC is bridged, the electric field in (3) is replaced by the applied anode

voltage multiplied by a fitting parameter, because there is no longer a gap between the

electrodes with which to calculate electric field. An electric field must still exist in order

to grow and dissolve the filament radius. Similar to (3), the ionic hopping current density

for the on-state is

$$j_{hop\_on} = 2zecaf(-\frac{W_a}{kT})\sinh(\frac{V \cdot \beta \cdot ze \cdot a}{2kT}) \tag{23}$$

where β is the electric field fitting parameter with units of cm$^{-1}$. In the on-state, the

filament radius after a time step, *dt*, is given by

$$r_{n+1} = r_n\sqrt{\frac{dt \cdot j_{hop\_on}}{(LzqN_{Ag})} + 1} \tag{24}$$

where $r_{n+1}$ is the radius after *dt*, and $r_n$ is the radius before *dt*. The model assumes an

initial radius of 2 nm. Once the filament bridges, the radius quickly grows until the

resistance is reduced to where the current becomes limited and the voltage drops below

the threshold for electrodeposition. A larger current limit allows the resistance to drop

lower since the threshold for electrodeposition is fixed. This is why the ON resistance

varies inversely with the compliance current limit. While the Butler-Volmer equation (2) is actually responsible for electrodeposition and electrodissolution, the model implements those thresholds in a much simpler and direct way. The ionic hoping current is only allowed when the applied voltage is above the set electrodeposition threshold ($V_{fwd}$) or below the set electrodissolution threshold ($V_{rev}$). Implementation of (2) into the numerical model should be preferred in the future.

The parameters used in the filament growth equations (3), (19–24) and the electro-deposition/dissolution thresholds are reported in Table VI.

Table VI:  Parameters for filament growth

| Parameter | Value | Unit | Description |
| --- | --- | --- | --- |
| $k$ | 8.617E-5 | eV/K | Boltzmann constant |
| $ze$ | 1.602E-19 | C | Charge per ion |
| $2zecaf$ | 5.379E3 | A/cm$^2$ | Mott-Gurney lumped coefficient |
| $a$ | 6E-8 | cm | Effective hopping distance |
| $W_{a\_fwd}$ | 0.310 | eV | Forward hopping activation energy |
| $W_{a\_rev}$ | 0.206 | eV | Reverse hopping activation energy |
| $T_0$ | 295 | K | Equilibrium temperature |
| $R_{th}$ | 1.0E5 | K/W | Thermal resistance |
| $N_A$ | 6.022E23 | mol$^{-1}$ | Avogadro constant |
| $\rho_{Ag2Se}$ | 8.216 | g/cm$^3$ | Ag$_2$Se density |
| $m_{Ag2Se}$ | 294.7 | g/mol | Ag$_2$Se molar mass |
| $N_{Ag}$ | 3.358E22 | cm$^{-3}$ | Ag concentration in filament |
| $\beta$ | 0.6 | cm$^{-1}$ | E-field fitting parameter |
| $V_{fwd}$ | 0.1 | V | Electrodeposition threshold |
| $V_{rev}$ | -0.05 | V | Electrodissolution threshold |

## 4.4. Compliance Current Implementation

Compliance current is the maximum allowable electrical current to a device under test. The Agilent 4156C has a compliance current setting to limit the current supplied to the device under test. A PMC is usually tested with compliance current to prevent overheating and to set different values of resistance. That same type of current limiting is needed in the numerical model so the same tests can be simulated.

Current is limited by reducing the applied voltage. In the numerical model, the voltage is constant during each time step. The model performs compliance checks and adjustments at the beginning and end of each time step. If the current exceeds compliance at the beginning of the step, then the reduced voltage is calculated to yield compliance by

$$V = I_{comp} \cdot R \cdot sgn(V_{in}) \qquad (25)$$

where $I_{comp}$ is the compliance current and $V_{in}$ is the unadjusted input voltage used to get the sign of the voltage. The filament can grow during the time step thereby decreasing the resistance and possibly causing the current to exceed the limit by the end of the step. Therefore, the current cannot be maintained exactly at the limit. A tolerance of 1% of the compliance current is allowed in the model. If the current exceeds compliance plus tolerance at the end of the step, then the time step, $dt$, is halved until the current remains in compliance at the end of the step.

## 4.5. Simulation Results

The simulated input, Fig. 20, is a triangle wave function that performs the double voltage sweep starting at 0V with a ramp rate of $\pm 1$ V/s with a maximum time step of 2 ms. $V_{in}$ is the user-defined input function and $V$ is the compliance adjusted function.
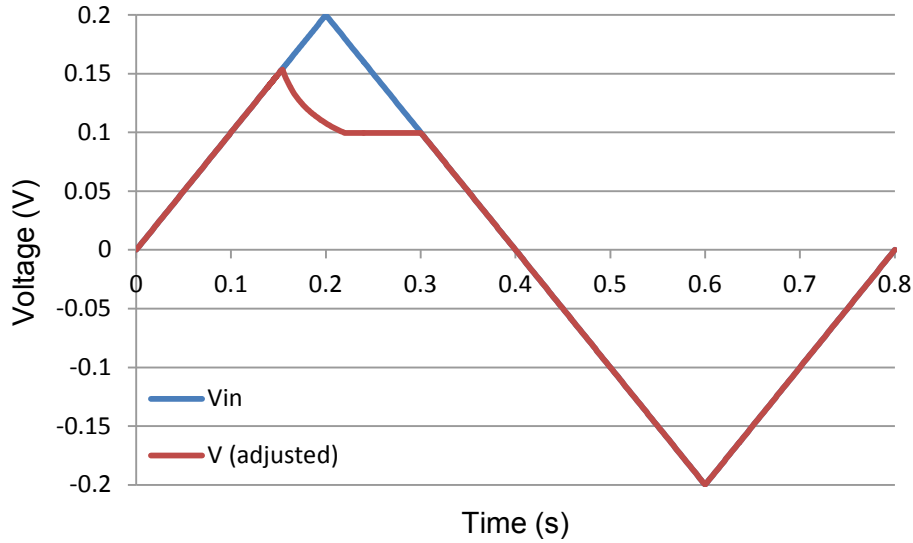


Fig. 20: Simulated piecewise linear function voltage input

The I-V characteristic is plotted alone on a linear y-scale in Fig. 21 and overlaid on the ASU PMC data plot of Fig. 5 in Fig. 22. These plots show an excellent match between the model and entire data curve. Notice that the curve has a kink in the programming switch as is sometimes observed in measured data. The first jump in the current occurs when a filament bridges the electrodes, but the resistance is not small enough to maximize the current. From there, the girth of the filament increases until the resistance drops enough to maximize the current. Once the current is limited, the voltage will drop below the minimum for electrodeposition and the filament will cease growth.
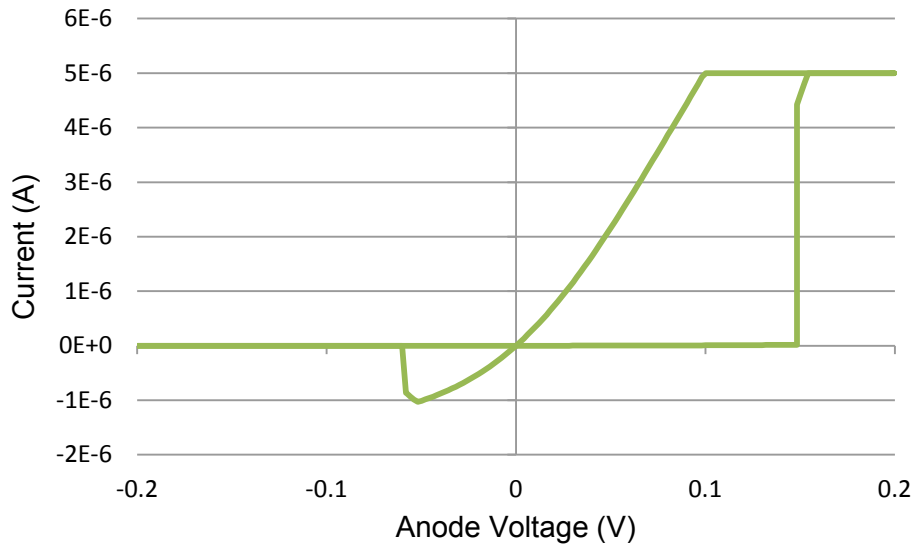
Fig. 21: Numerical model I-V characteristic on a linear y-scale
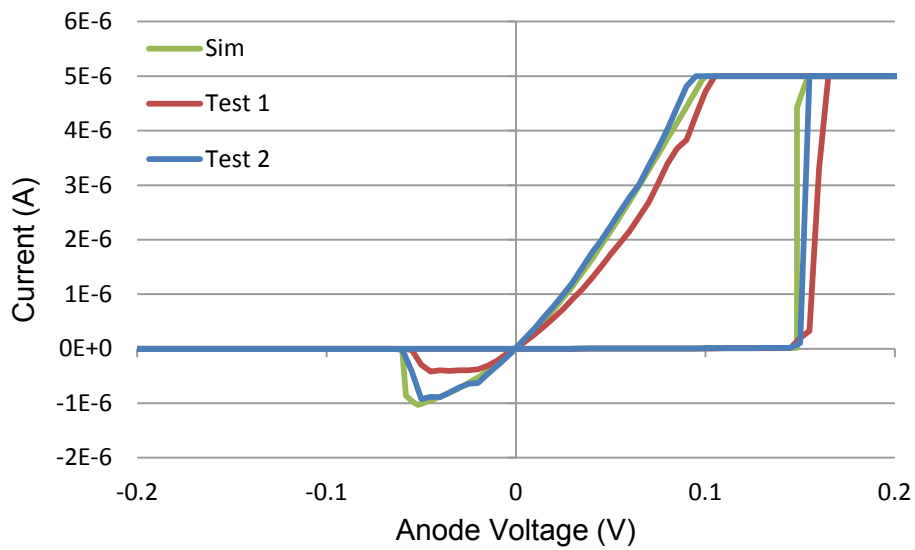


Fig. 22: Linear I-V numerical model data overlaid on ASU PMC data

The I-V characteristic is plotted alone on a logarithmic y-scale in Fig. 23 and overlaid on the ASU PMC data plot of Fig. 6 in Fig. 24. These plots show an excellent match of the current at orders of magnitude.
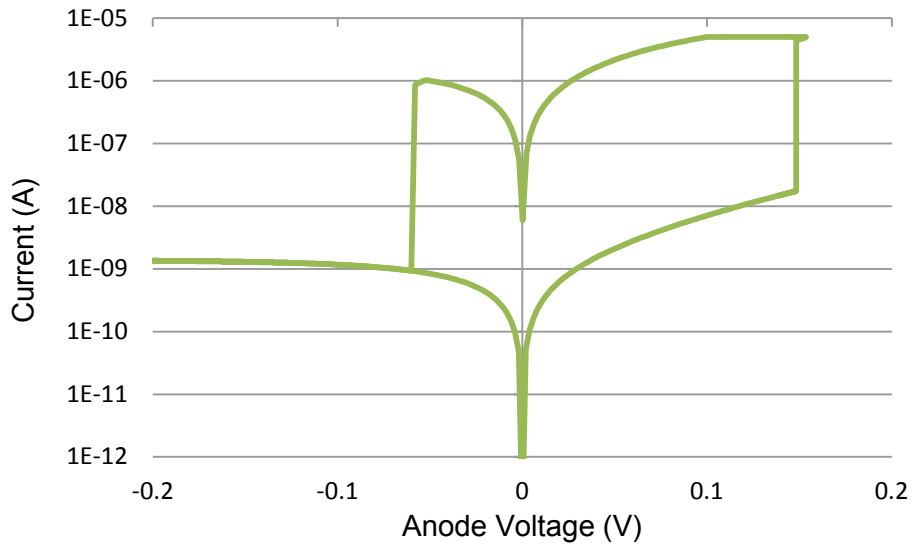
Fig. 23: Numerical model I-V characteristic on a logarithmic y-scale
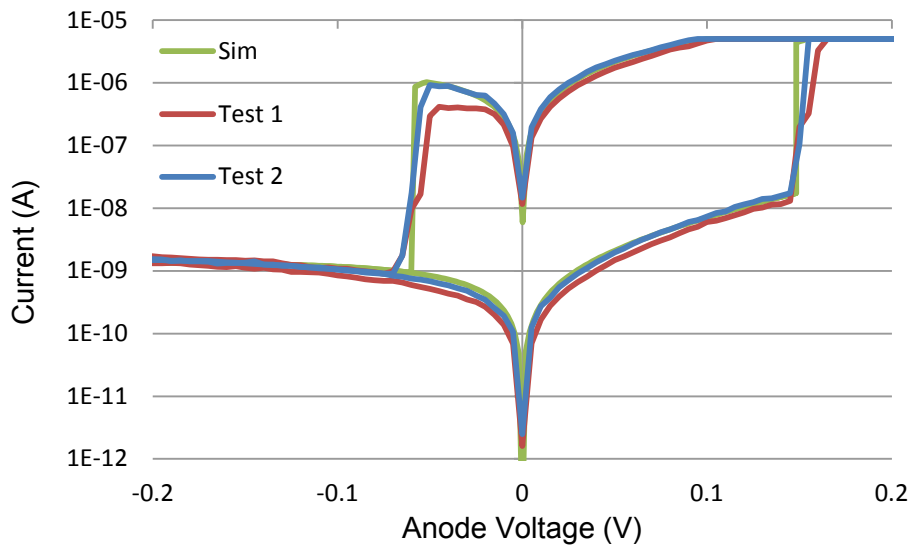


Fig. 24: Logarithmic I-V numerical model data overlaid on ASU PMC data

The R-V characteristic is plotted alone in Fig. 25 and overlaid on the ASU PMC

data plot of Fig. 7 in Fig. 26. These plots show a very good match of the resistance at all

levels. The "unadjusted" resistance shown in Fig. 25 is the resistance calculated with the unadjusted input voltage as is done with measured data. The model is able to show the real R-V characteristic even where the current is limited.
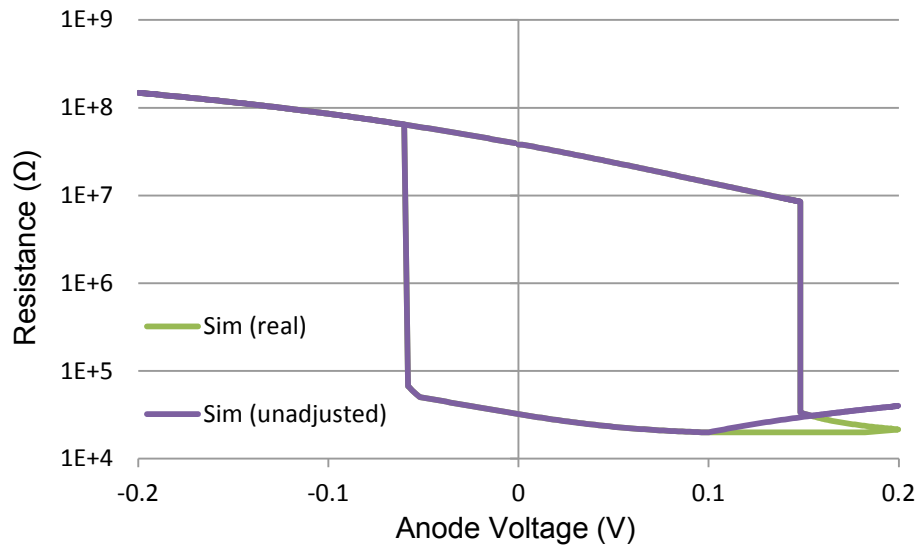


Fig. 25: Numerical model R-V characteristic
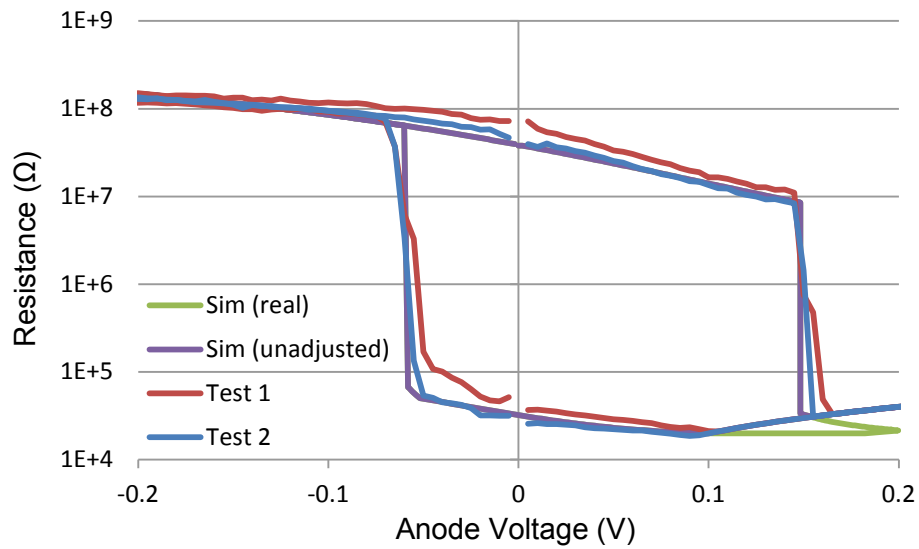


Fig. 26: R-V numerical model data overlaid on ASU PMC data

Table VII provides a quantitative comparison of key I-V characteristics between the ASU PMC Test 2 data and the numerical model. The percentage errors are fairly small, and they could be further reduced with better parameter fitting. The parameters of the numerical model were quickly adjusted for an approximate match by visual comparison of the plotted I-V data on a logarithmic scale. However, PMCs are currently not precision devices. These values vary between PMC devices of the same design and even between measurements of a single device. Therefore, fitting the model near exactly with data from a single measurement may be of little importance.

Table VII:  Quantitative comparison of ASU PMC and Numerical Model

|  | $R_{OFF}$ ($\Omega$) @ 10 mV | $R_{ON}$ ($\Omega$) @ 10 mV | $V_{write}$ (mV) | $V_{erase}$ (mV) |
|---|---|---|---|---|
| ASU PMC Test 2 | 3.664E+07 | 2.622E+04 | 150.0 | -60.00 |
| Numerical Model | 3.530E+07 | 2.975E+04 | 148.3 | -60.10 |
| Percent Error | -3.657 | 13.46 | -1.13 | 0.17 |

A parametric simulation was also performed where only the compliance current limit was varied. Fig. 27 plots the I-V curves with compliance currents of 1 μA, 5 μA and 10 μA. Fig. 28 plots the corresponding R-V curves. These results demonstrate the multilevel programmability of the numerical model. A greater compliance current allows the filament radius to increase more and the resistance to decrease more until the minimum electrodeposition voltage divided by the resistance equals the greater compliance current. Notice that all three curves drop out of the limited current regime at

0.1V, because that is the electrodeposition threshold which determines the set resistance according to (1). The results also show that larger filaments require more negative voltage-time to dissolve.
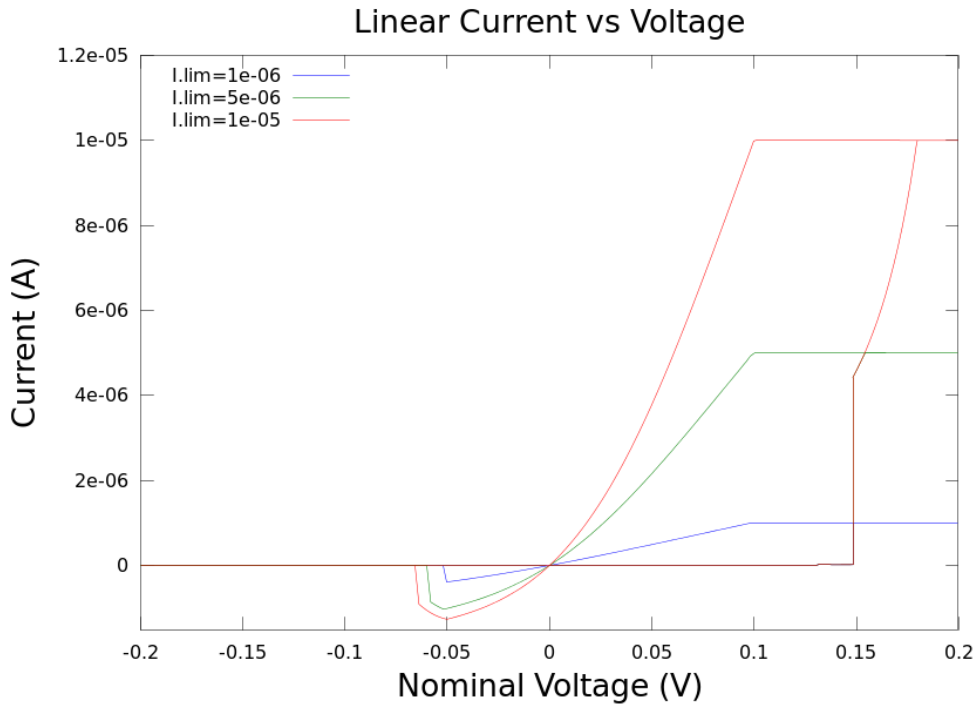


Fig. 27:  I-V simulation with parametric compliance current
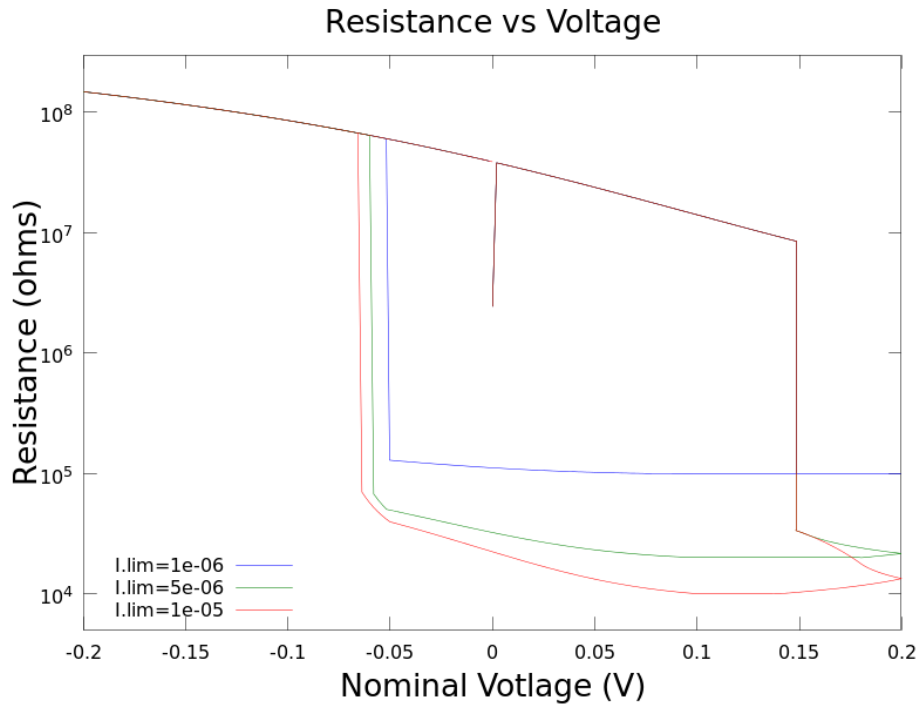
Fig. 28: R-V simulation with parametric compliance current

The simulation results of the physics-based numerical model are shown to
effectively model the ASU PMC. The numerical model offers greater insight into the
parameters and operation of the PMC. The possible effects of varied parameters and
equations are easily observable. Several of the parameters were fit to the data for these
results; however, the model can be refined with more measured and calculated
parameters instead of fitted parameters to see how the model holds up. Comparison of the
model with different PMC tests can be performed to further adjust and validate the
model. A future improvement would be to add the Butler-Voltage charge transfer
equation.

## 5. CONCLUSION

This thesis has presented the modeling efforts and results of a novel finite element model and a numerical model. The FEA software used for the finite element model turned out to be incapable of modeling filament formation in the PMC. Specifically, the generic ion transport and reaction models were not developed with the ability to model the conductive filament growth. The workaround devised to convert the non-conducting neutral species into donors was able to achieve a resistance change NVM characteristic; however, the operating mechanism remained vastly inconsistent with a PMC. The reasons why the finite element model does not work have been reported.

A physics-based numerical model has been successfully implemented and tested with great results. The simulation results show an outstanding match in all aspects of the I-V and R-V characteristics of a ChG-based ASU PMC. This model has the ability to simulate multilevel programming, various input waveforms and quick parametric sweeps, which provide the observer with a greater insight into the detailed operation of the PMC. For example, the model may be used to predict pulsed mode and low- or high-temperature operation. With further refinements of the material properties and possibly additional physics such as the Butler-Volmer charge transfer equation, the model could become further validated and predict the characteristics of modified PMC designs. At that point, the model could aid in designing optimized PMCs or provide the insight for developing application specific compact models.

REFERENCES

[1]     K. Sudan, A. Badam and D. Nellans, "NAND-flash: Fast storage or slow
        memory?" in *Non-Volatile Memories Workshop,* San Diego, 2012.

[2]     F. Masuoka, M. Asano, H. Iwahashi, T. Komuro and S. Tanaka, "A new flash
        E$^2$PROM cell using triple polysilicon technology," in *Electron Devices Meeting,
        1984 International,* 1984, pp. 464-467.

[3]     (March 27, 2013). *ioDrive Octal Data Sheet.* Available:
        http://www.fusionio.com/load/-media-/24drmm/docsLibrary/FIO_DS_Octal.pdf.

[4]     (February 14, 2013). *Micron Introduces Industry's Smallest 128-Gigabit NAND
        Flash Device.*

[5]     "ITRS 2012 update overview," International Technology Roadmap for
        Semiconductors, 2012.

[6]     "ITRS Emerging research devices," International Technology Roadmap for
        Semiconductors, 2011.

[7]     J. Hutchby and M. Garner, "Assessment of the potential & maturity of selected
        emerging research memory technologies," International Technology Roadmap for
        Semiconductors, 2010.

[8]     I. Valov, R. Waser, J. R. Jameson and M. N. Kozicki, "Electrochemical
        metallization memories—fundamentals, applications,
        prospects," *Nanotechnology,* vol. 22, pp. 254003, 2011.

[9]     M. Suri, O. Bichler, D. Querlioz, G. Palma, E. Vianello, D. Vuillaume, C. Gamrat
        and B. DeSalvo, "CBRAM devices as binary synapses for low-power stochastic
        neuromorphic systems: Auditory (cochlea) and visual (retina) cognitive
        processing applications," in *Electron Devices Meeting (IEDM), 2012 IEEE
        International,* 2012, pp. 10.3.1-10.3.4.

[10]    S. R. Baliga, M. Ren and M. N. Kozicki, "Self-healing interconnects for flexible
        electronics applications," *Thin Solid Films,* vol. 519, pp. 2339-2343, 1/31, 2011.

[11]    L. Gao, F. Alibart and D. B. Strukov, "Programmable CMOS/Memristor
        Threshold Logic," *Nanotechnology, IEEE Transactions On,* vol. 12, pp. 115-119,
        2013.

[12]    S. Je, J. Kim, J. C. Harrison, M. N. Kozicki and J. Chae, "In situ tuning of
        omnidirectional microelectromechanical-systems microphones to improve

performance fit in hearing aids," *Appl. Phys. Lett.,* vol. 93, pp. 123501, 22 September 2008, 2008.

[13]    M. N. Kozicki, P. Maroufkhani and M. Mitkova, "Flow regulation in microchannels via electrical alteration of surface properties," *Superlattices and Microstructures,* vol. 34, pp. 467-473, 0, 2003.

[14]    M. Mitkova, M. N. Kozicki, H. C. Kim and T. L. Alford, "Crystallization effects in annealed thin Ge–Se films photodiffused with Ag," *J. Non Cryst. Solids,* vol. 352, pp. 1986-1990, 6/15, 2006.

[15]    M. Kund, G. Beitel, C. -. Pinnow, T. Rohr, J. Schumann, R. Symanczyk, K. -. Ufert and G. Muller, "Conductive bridging RAM (CBRAM): An emerging non-volatile memory technology scalable to sub 20nm," in *Electron Devices Meeting, 2005. IEDM Technical Digest. IEEE International,* 2005, pp. 754-757.

[16]    S. Dietrich, M. Angerbauer, M. Ivanov, D. Gogl, H. Hoenigschmid, M. Kund, C. Liaw, M. Markert, R. Symanczyk, L. Altimime, S. Bournat and G. Mueller, "A Nonvolatile 2-Mbit CBRAM Memory Core Featuring Advanced Read and Program Control," *Solid-State Circuits, IEEE Journal Of,* vol. 42, pp. 839-845, 2007.

[17]    N. Derhacobian, S. C. Hollmer, N. Gilbert and M. N. Kozicki, "Power and Energy Perspectives of Nonvolatile Memory Technologies," *Proceedings of the IEEE,* vol. 98, pp. 283-298, 2010.

[18]    A. S. Oblea, A. Timilsina, D. Moore and K. A. Campbell, "Silver chalcogenide based memristor devices," in *Neural Networks (IJCNN), the 2010 International Joint Conference On,* 2010, pp. 1-3.

[19]    I. Valov and M. N. Kozicki, "Cation-based resistance change memory," *J. Phys. D,* vol. 46, pp. 074005, 2013.

[20]    A. H. Edwards and K. A. Campbell, "Density functional study of ag in $Ge_2Se_3$," in *Non-Volatile Memory Technology Symposium (NVMTS), 2009 10th Annual,* 2009, pp. 1-7.

[21]    U. Russo, D. Kamalanathan, D. Ielmini, A. L. Lacaita and M. N. Kozicki, "Study of Multilevel Programming in Programmable Metallization Cell (PMC) Memory," *Electron Devices, IEEE Transactions On,* vol. 56, pp. 1040-1047, 2009.

[22]    R. Waser, "Redox-Based Resistive Switching Memories - Nanoionic Mechanisms, Prospects, and Challenges," *Adv. Mater.,* vol. 21, pp. 2632-2663, Jul. 13, 2009.

[23] A. J. Bard and L. R. Faulkner, *Electrochemical Methods :Fundamentals and Applications.* New York: Wiley.

[24] N. F. Mott and R. W. Gurney, *Electronic Processes in Ionic Crystals.* Oxford : Clarendon Press, 1948.

[25] J. J. O'Dwyer, *The Theory of Electrical Conduction and Breakdown in Solid Dielectrics.* Oxford: Clarendon Press, 1973.

[26] S. Yu and H. -. P. Wong, "Compact Modeling of Conducting-Bridge Random-Access Memory (CBRAM)," *Electron Devices, IEEE Transactions On,* vol. 58, pp. 1352-1360, 2011.

[27] Y. Hirose and H. Hirose, "Polarity-dependent memory switching and behavior of Ag dendrite in Ag-photodoped amorphous $As_2S_3$ films," *J. Appl. Phys.,* vol. 47, pp. 2767-2772, June, 1976.

[28] X. Guo, C. Schindler, S. Menzel and R. Waser, "Understanding the switching-off mechanism in $Ag^+$ migration based resistively switching model systems," *Appl. Phys. Lett.,* vol. 91, pp. 133513, Sept. 24, 2007.

[29] C. Hsiung, H. Liao, J. Gan, T. Wu, J. Hwang, F. Chen and M. Tsai, "Formation and Instability of Silver Nanofilament in Ag-Based Programmable Metallization Cells," *ACS Nano,* vol. 4, pp. 5414-5420, Aug. 13, 2010.

[30] N. Terakado and K. Tanaka, "Electrical responses of chalcogenide films in the photodoping process," *Thin Solid Films,* vol. 519, pp. 3773-3777, 3/31, 2011.

[31] H. Barnaby, A. Edwards, D. Oleksy and M. N. Kozicki, "Finite element modeling of ag transport and reactions in chalcogenide glass resistive memory," in *Proceedings of the 2013 IEEE Aerospace Conference,* 2013.

[32] H. Jonsson, G. Mills and K. W. Jacobsen, "Nudged elastic band method for finding minimum energy paths of transitions," in Anonymous World Scientific, 1998, pp. 385-404.

[33] M. C. S. Kumar and B. Pradeep, "Electrical properties of silver selenide thin films prepared by reactive evaporation," *Bull. Mater. Sci.,* vol. 25, pp. 407-411, 10/01, 2002.

[34] D. Ielmini, "Filamentary-switching model in RRAM for time, energy and scaling projections," in *Electron Devices Meeting (IEDM), 2011 IEEE International,* 2011, pp. 17.2.1-17.2.4.

[35]     U. Russo, D. Ielmini, C. Cagli and A. L. Lacaita, "Self-Accelerated Thermal
         Dissolution Model for Reset Programming in Unipolar Resistive-Switching
         Memory (RRAM) Devices," *Electron Devices, IEEE Transactions On,* vol. 56,
         pp. 193-200, 2009.

APPENDIX A

FINITE ELEMENT MULTIPART SIMULATION

This is a description of the workaround for the Atlas generic ion model. This workaround splits a standard transient simulation into multiple parts so that the neutral species can be copied into donors between parts. An input deck is a file with a list of commands giving Atlas the problem to solve. Normally, a single input deck is all that is required to run a simulation. The key functions of the initial input deck, Fig. 29, are to define the initial PMC structure, the initial sp1 doping profile, and begin the simulation with the equilibrium solution. This input deck saves the resulting structure file, which is a solution of the structure with 0V applied. This solution redistributes the ionic species into an equilibrium state.

The running input deck, Fig. 30, is used to continue the simulation for each of the remaining simulation parts after the first. The deck loads the structure saved from the initial input deck. Three doping files, generated by a Python script (Figs. 31–33) with the previous solution structure, are used to dope the current structure with sp0, sp1, and donors matching the profile of sp0. The final difference in the running input deck is the solve statement. Instead of solving with 0V applied, a short transient voltage ramp from the previous to next voltage is simulated. First, the structure is solved at the previous voltage while freezing the species so they cannot move. This provides the starting point for the voltage sweep. Lastly, the voltage ramps up to the next value.

A Python script, Figs. 31–33, generates new doping profiles before and between each execution of the running input deck. This script reads the output structure from the previous simulation. The doping concentrations of sp0 and sp1 are recorded at every coordinate in the structure. Then, the script writes three separate .lib files written in C that provide the doping profiles of sp0, sp1 and donors for the next simulation part. Atlas has

a C-interpreter that reads the .lib files to set the doping concentrations at every coordinate in the structure.

An AWK script, Fig. 34, is also used to update the running input deck with the new voltage between simulations for the voltage ramp to continue. The running input deck utilizes variables for the previous and next voltage. The AWK script is supplied with the variable values and executed by an automating Python script.

The automating Python script, Fig. 35, automates the execution of this complex multipart simulation. The user provides this script with the final voltage of the ramp and the number of steps to divide it into. Then, the script executes the initial input deck. Next, the script enters a loop which begins with setting the previous and next voltages. Then, the AWK script is supplied with those values and executed to update the running input deck. Then, the doping Python script is executed to generate the three .lib files. The last piece of the loop is the execution of the running input deck. The multipart simulation is complete when this loop completes its iterations. The input decks save solution structures at each part. The results are viewed by opening those structures in Silvaco TonyPlot.

```
 1    go atlas
 2    set vanode=0
 3    # define structure mesh and materials
 4    mesh width=1.0
 5    x.m loc=0.0 spac=0.01
 6    x.m loc=1.0 spac=0.01
 7    y.m loc=0.0 spac=0.001
 8    y.m loc=0.05 spac=0.001
 9    region num=1 silicon y.max=0.05
10    electrode name=anode top
11    electrode name=cathode bottom
12    # set initial ion doping profile
13    doping region=1 species1 uniform conc=1e18 y.max=0.01
14    contact name=anode workfunction=4.6
15    contact name=cathode workfunction=4.2
16    # species 1 is Ag+
17    material species1.hop=1e-6 species1.af=1e15 species1.ea=0.25
18    # species 2 is Ag
19    material species2.hop=1e-10 species2.af=1e4 species2.ea=1.5
20    # set material parameters for electrolyte
21    material region=1 eg300=2.5 nc300=1e19 nv300=1e19 mun=100 mup=100
      permittivity=5 affinity=3.45 taun0=1 taup0=1
22    # set model(s) and species charges
23    models srh nspecies=2 species1.z=1 species2.z=0
24    # specify reactions
25    reaction before.sp1=1 before.n=1 after.sp2=1 forward.rate=1e2
      forward.ea=0.5 reverse.rate=1e-10 reverse.ea=1.0
26    # set models and outputs
27    method gummel species.maxx=1.0e6
28    output charge band.param con.band val.band
29    # get initial solution
30    solve init
31    save outf=str/pmc_init.str master
32    # simulate 0V bias for some time
33    log outf=log/pmc_$"vanode".log
34    solve vanode=$"vanode" dt=1e-13 tstop=1e-11
35    solve vanode=$"vanode" dt=1e-9 tstop=10e-6
36    save outf=str/pmc_$"vanode".str master
37    quit
```

Fig. 29:  Initial input deck for Atlas simulation

```
 1   go atlas
 2   # set previous and next anode voltages
 3   set vanode_prev= 0
 4   set vanode= 0.1
 5   # load device structure/mesh from initial structure
 6   mesh inf=str/pmc_init.str
 7   # set doping profiles from python generated files
 8   doping name=chg species1 f.doping=doping_sp1.lib
 9   doping name=chg species2 f.doping=doping_sp2.lib
10   doping name=chg p.type f.doping=doping_n.lib
11   contact name=anode workfunction=4.6
12   contact name=cathode workfunction=4.2
13   # species 1 is Ag+
14   material species1.hop=1e-6 species1.af=1e15 species1.ea=0.25
15   # species 2 is Ag
16   material species2.hop=1e-10 species2.af=1e4 species2.ea=1.5
17   # set material parameters for electrolyte
18   material region=1 eg300=2.5 nc300=1e19 nv300=1e19 mun=100 mup=100
     permittivity=5 affinity=3.45 taun0=1 taup0=1
19   # set model(s) and species charges
20   models srh nspecies=2 species1.z=1 species2.z=0
21   # specify reactions
22   reaction before.sp1=1 before.n=1 after.sp2=1 forward.rate=1e2
     forward.ea=0.5 reverse.rate=1e-10 reverse.ea=1.0
23   # set models and outputs
24   method gummel species.maxx=1.0e6
25   output charge band.param con.band val.band
26   # get initial solution with frozen species
27   solve vanode=$"vanode_prev" freezespecies
28   # simulate voltage ramp
29   log outf=log/pmc_$"vanode".log
30   solve vanode=$"vanode" dt=1e-8 tstop=10e-6 ramptime=1e-6
31   save outf=str/pmc_$"vanode".str master
32   quit
```

Fig. 30:  Running input deck for Atlas simulation

```python
#!/usr/bin/python
import re, os, string, sys

def makeLibs(structure_file, id):
    struct = open(structure_file,'r')
    sp1 = open('doping_sp1.lib','w')
    sp2 = open('doping_sp2.lib','w')
    sp3 = open('doping_n.lib','w')
    s = 1
    x = []
    y = []
    n_sp1 = []
    n_sp2 = []
    strt=struct.readlines()
    for line in strt:
      p=line.split()
      if p[0] == 'c':
        x.append(p[2])
        y.append(p[3])
      elif p[0] == 's':
        for num in p:
          if eval(num) == 71:
            idx_donor_conc = s
          elif eval(num) == 72:
            idx_acceptor_conc = s
          elif eval(num) == 106:
            idx_electron_conc = s
          elif eval(num) == 107:
            idx_hole_conc = s
          elif eval(num) == 115:
            idx_net_doping_conc = s
          elif eval(num) == 116:
            idx_charge_conc = s
          elif eval(num) == 149:
            idx_total_doping_conc = s
          elif eval(num) == 853:
            idx_species1_conc = s
          elif eval(num) == 854:
            idx_species2_conc = s
          elif eval(num) == 855:
            idx_species3_conc = s
          s = s+1
```

Fig. 31: Python script to generate doping profile files (1/3)

```python
43      elif p[0] == 'n':
44          n_sp1.append(p[idx_species1_conc])
45          n_sp2.append(p[idx_species2_conc])
46
47      sp1.write("#include <stdio.h>\n#include
        <stdlib.h>\n#include <math.h>\n#include <ctype.h>\n#include
        <malloc.h>\n#include <string.h>\n#include <template.h>\nint
        doping(double x, double y, double *nnet){\n")
48      sp2.write("#include <stdio.h>\n#include
        <stdlib.h>\n#include <math.h>\n#include <ctype.h>\n#include
        <malloc.h>\n#include <string.h>\n#include <template.h>\nint
        doping(double x, double y, double *nnet){\n")
49      sp3.write("#include <stdio.h>\n#include
        <stdlib.h>\n#include <math.h>\n#include <ctype.h>\n#include
        <malloc.h>\n#include <string.h>\n#include <template.h>\nint
        doping(double x, double y, double *nnet){\n")
50
51      i = 0
52      xx = []
53      yy = {}
54      for b in x:
55          if not b in xx:
56              xx.append(b)
57              yy[b] = [y[i]]
58          else:
59              yy[b].append(y[i])
60          i = i+1
61
62      i = 0
63      delta = 1e-10
64
65      for b in xx:
66          sp1.write("  if(x>"+str(eval(b)-delta)+" && x<"+str(eval(b
        )+delta)+"){\n")
67          sp2.write("  if(x>"+str(eval(b)-delta)+" && x<"+str(eval(b
        )+delta)+"){\n")
68          sp3.write("  if(x>"+str(eval(b)-delta)+" && x<"+str(eval(b
        )+delta)+"){\n")
```

Fig. 32: Python script  to generate doping profile files (2/3)

57

```
69    for a in yy[b]:
70      sp1.write("    if(y>"+str(eval(a)-delta)+" && y<"+str(
        eval(a)+delta)+")\n         *nnet="+n_sp1[i]+";\n")
71      sp2.write("    if(y>"+str(eval(a)-delta)+" && y<"+str(
        eval(a)+delta)+")\n         *nnet="+n_sp2[i]+";\n")
72      Nd = n_sp2[i]
73      sp3.write("    if(y>"+str(eval(a)-delta)+" && y<"+str(
        eval(a)+delta)+")\n         *nnet="+Nd+";\n")
74      i = i+1
75    sp1.write("  }\n")
76    sp2.write("  }\n")
77    sp3.write("  }\n")
78
79  sp1.write("  return(0);\n}")
80  sp2.write("  return(0);\n}")
81  sp3.write("  return(0);\n}")
82  sp1.close()
83  sp2.close()
84  sp3.close()
85  os.system('cp -f doping_n.lib doping/doping_n_'+str(id)+
        '.lib')
```

Fig. 33: Python script to generate doping profile files (3/3)

```
1  {
2      if( $1 == "set" && $2 == "vanode=" ) {
3          $3 = vanode;
4          printf "%s %s %1.3f\n", $1, $2, $3;
5      }
6      else {
7          print;
8      }
9  }
```

Fig. 34: Awk script to update the running deck

```python
#!/usr/bin/python
import re, os, string, sys, doping

# user input next two lines:
v_final = 1.0
v_steps = 10

spv = v_steps / v_final
vanode_prev = 0
vanode = 0
seq = range(1, int(v_steps)+1)

os.system('/silvaco_3202012/bin/deckbuild -run -ascii -as
initial_deck.in -outfile history.log')

for i in seq:
    vanode = i / spv
    vanode = '%g'%(vanode)
    if vanode != 0:
        vanode_prev = (i - 1) / spv
    vanode_prev = '%g'%(vanode_prev)
    print vanode_prev+' of '+str(v_final)+' V'
    os.system('awk -f update_deck.awk vanode='+vanode+'
    vanode_prev='+vanode_prev+' running_deck.in > updated.in')
    os.system('mv -f updated.in running_deck.in')
    doping.makeLibs('str/pmc_'+vanode_prev+'.str',
    vandode_prev)
    os.system('/silvaco_3202012/bin/deckbuild -run -ascii
    -as running_deck.in -outfile history.log')

print str(v_final)+' of '+str(v_final)+' V'
print 'Simulation Completed.'
```

Fig. 35:  Python script to automate multipart simulation